

Development of an EGFR-targeted Drug Delivery System for Glioblastoma

by

Ziruo Zhao

BSc. (Hons.)

Supervised by

Professor Neil R. Thomas

Dr Tracey D. Bradshaw

Thesis submitted to the University of Nottingham for the degree of Master of Research (School of Chemistry)

October 2022

Abstract

Glioblastoma (GB) is one of the most malignant cancers with a dismal survival of 4 months when no treatment intervenes. After standard of care: surgery, radiotherapy and temozolomide (TMZ) chemotherapy, its median survival has been increased to 16 months. TMZ functions by methylating guanine of GB DNA into O^6-methylguanine, which triggers a futile cycle of base excision-reinsertion conducted by DNA mismatch repair mechanism (MMR), eventually leading to DNA-strands breakdown and cell apoptosis. However, TMZ efficacy is largely limited by factors such as poor in-brain accumulation due to low level permeation across the blood-brain barrier, and O^6-methylguanine-DNA methyltransferase (MGMT) which reverses the guanine methylation. The natural transportation protein apoferritin (AFt) shapes as a spherical hollow nanocage and has been proven to be a biocompatible drug delivery vehicle. It possesses 3-4 Å surface channels available for the entrance of iron ions and small molecules and allows modification at its N-termini on the exterior surface with different moieties. The overexpression of epidermal growth factor receptor (EGFR) is often observed in GB and can be seen as a biomarker; while the anti-EGFR affibodies, which are small affinity molecules of strong binding-affinity towards specific target, have been developed for many research purposes, an EGFR-affibody directed AFt delivery system is proposed to promote the performance of TMZ against GB.

This study aimed to exploit *E. coli* protein expression to produce recombinant human heavy chain AFt (human H-AFt) and its derivative with 24 EGFR-affibodies fused at N-termini (EGFRa@AFt) to encapsulate TMZ molecules (~500/cage), constructing the drug delivery systems AFt-TMZ and EGFRa@AFt-TMZ. Upon MTT viability assays (72 h), against EGFR-overexpressed GB cell line U373V, EGFRa@AFt-TMZ system exhibited significantly enhanced growth inhibition with GI_{50} of 8.18 ± 1.67 pM, which was lower than AFt-TMZ system and free TMZ molecules by ~3 and 7 orders of magnitudes, respectively ($P < 0.0001$); while the growth of non-tumourigenic control human fibroblast MRC-5 cell line was negligibly compromised at concentrations < 20 nM. These suggested an *in vitro* targeting ability and enhanced drug activity of EGFRa@AFt-TMZ system. The similar responses between U373V and MGMT- transfected isogenic U373M cell line suggested its potential to overcome MGMT-mediated resistance to TMZ. However, the EGFR-overexpressed and MMR-deficient HCT-116 colon cancer cell line responded to both EGFRa@AFt-TMZ and AFt-TMZ systems at an equivalent level, suggesting that the effectiveness of TMZ might be limited by MMR level.

Acknowledgement

Here, I, from all my heart:

Sincerely express my gratitude for the help from my supervisors,

Prof Neil Thomas and **Dr Tracey Bradshaw**,

for their patience and efforts;

and thanks to **all friends from A20 lab**,

for they guided me alongside my research life;

as well **my beloved parents** who love me too,

though you guys probably will never read this thesis,

and are still quite unsure

about where I live, or what I do.

I wish you all the rings of Saturn, the splash of wave,

and health for good.

Abbreviations & Acronyms

AFt	apoferritin
AFt-TMZ	human heavy chain apoferritin encapsulated with TMZ
AIC	4-amino-5-immidazole-carboxamide
BSA	bovine serum albumin
CNS	central nervous system
CT	computed tomography
Da	Dalton
DNA	deoxyribonucleic acid
dH_2O	deionised water
DMSO	dimethyl sulfoxide
DTT	Dithiothreitol
ECL	enhanced chemiluminescence
EDTA	ethylenediaminetetraacetic acid
EGFR	epidermal growth factor receptor
EGFRa@AFt	EGFR-affibody N terminal fused apoferritin
EGFRa@AFt-TMZ	EGFRa@AFt encapsulated with temozolomide
FBS	fetal bovine serum
g	gram
g	gravity
GAPDH	glyceraldehyde 3-phosphate dehydrogenase
GB	glioblastoma
GI_{50}	growth-inhibitory ability of 50% inhibition
h	hours
human H-AFt	human heavy chain apoferritin
IMS	industrial methylated spirit
indirect ELISA	indirect enzyme-linked immunosorbent assay
ITPG	isopropyl β-D-1-thiogalactopyranoside
k	kilo
kDa	kilodalton
L	litre
LC 3	light chain 3

LPS	lipopolysaccharide
m	milli
MGMT	O^6-methylguanine-DNA methyltransferase
min	minutes
milli-Q water	ultra-pure deionised water
MMR	mismatch repair
MRI	scan and magnetic resonance imaging
MTT	3-(4,5-dimethylthiazol-2-yl)-2,5-diphenyltetrazolium bromide
MW	molecular weight
*N*3-MeA	N^3-methyladenine
N3P	TMZ analogue with N^3-methyl substituted by propargyl
*N*7-MeG	N^7-methylguanosine
NADPH	nicotinamide adenine dinucleotide phosphate
NaOH	sodium hydroxide
$NiSO_4$	nickel sulfate
NR	neutral red
OD	optical density
*O*6-MeG	O^6-Methylguanine
PAGE	polyacrylamide gel electrophoresis
PBS	phosphate buffered saline
pen/strep	penicillin/streptomycin
RIPA	radioimmunoprecipitation assay
SDS	sodium dodecyl-sulfate
S.O.C.	super optimal broth with catabolite repression
t_0/T_0	time zero (starting point)
TBST	tris-buffered saline with Tween20 detergent
TEMED	*N, N, N′, N′*-Tetramethyl ethylenediamine
TKD	tyrosine kinase domain
TMZ	temozolomide
TfR1	transferrin receptor 1
tris	trizma base
µ	micro
°C	degree Celsius

Catalogue

1. Introduction ····· 8

1.1 Glioblastoma (GB) ····· 8

1.1.1 Background ····· 8

1.1.2 Classification ····· 9

1.2.3 GB pathogenesis & treatments ····· 10

1.2 Temozolomide ····· 13

1.2.1 Characteristics ····· 13

1.2.2 Mechanism of action ····· 15

1.2.3 Challenges ····· 17

1.3 Apoferritin ····· 19

1.3.1 Background & Characteristics ····· 19

1.3.2 Biocompatible nano-cage ····· 21

1.4 EGFR: a biomarker of GB ····· 23

1.4.1 Receptor tyrosine kinases ····· 23

1.4.2 EGFR family (EGFRs) ····· 25

1.5 Affibody modified AFt: promising targeting drug delivery system ····· 28

1.5.1 Background ····· 28

1.5.2 EGFR affibody-AFt fusion protein ····· 30

2. Objectives ····· 33

3. Methods ····· 34

3.1 Materials ····· 34

3.1.1 Chemical substances ····· 34

3.1.2 DNA plasmids ····· 37

3.1.3 Cell lines & growth medium ····· 38

3.2 Protein expression in *E. coli* ····· 39

3.2.1 Transformation ····· 39

3.2.2 *E. coli* culture ····· 39

3.2.3 Protein extraction ····· 40

3.2.4 Sample purification ····· 41

3.3 Electrophoresis ····· 43

3.3.1 Gel preparation ····· 43

3.3.2 Performing electrophoresis ····· 45

3.4 Investigating TMZ stability 46
3.5 Encapsulation 47
3.5.1 Constructing EGFRa@AFt-TMZ system 47
3.5.2 Encapsulation mimetic 48
3.6 Mammalian Cell culture 49
3.6.1 Cells thawing 49
3.6.2 Cells passaging 49
3.6.3 Cells freezing 50
3.7 Cell assays 50
3.7.1 Cell counting 50
3.7.2 MTT viability assay 51
3.7.3 Clonogenic assay 53
3.8 Western blot 54
3.8.1 Collecting cell lysates 54
3.8.2 Bradford assay 55
3.8.3 Western blotting (Semi-dry transfer) 55
3.8.4 Antibody incubation and imaging 56
4. Results & discussion 57
4.1 Protein expression 57
4.1.1 Protein extraction 57
4.1.2 Purification results 58
4.2 Verification of encapsulation 61
4.2.1 TMZ stability curves 61
4.2.2 Structure integrity of EGFRa@AFt and human H-AFt 63
4.2.3 Encapsulation mimetic 64
4.3 EGFR expression 66
4.4 Cell assays 69
4.4.1 *In vitro* activity (MTT assay) 69
4.4.2 Colony formation of U373 cells 74
5. Conclusions & Future works 77
6. Reference 82
7. Appendix 98

1. Introduction

1.1 Glioblastoma (GB)

1.1.1 Background

Currently glioblastoma (GB; previously known as glioblastoma multiforme) is one of the most malignant carcinomas in the world threatening thousands of lives. It constitutes approximately 45.2% of Central nervous system (CNS) cancers, and by 2016 has reached a global incidence of 4.63 per 100,000 people annually [1]. Even after standard of care treatment, the overall survival is dismal with a median of only 16 months [2]. The short-term survival rate (2-3 years) has slightly improved over the last two decades (9% to 18%), yet the long-term survival (>5 years) remains less than 5% [3]. Statistics have shown the disease tends to occur and kill among the elderly population with a median age of 64-year-old and an increasing YLDs (years of healthy life lost due to disability) between 60- and 75-year-olds [4]. Males are generally more likely to develop GB than females and they also have a lower survival rate, suggesting that gender factors such as hormones may contribute to the disease development [5]. Currently, China, India, and the United States are three countries that suffer from the highest GB incidences [6]. The unsatisfying prognosis and rapid development have caused a heavy burden on patients worldwide.

1.1.2 Classification

The detailed classification of the disease contributes to more thorough investigations into individual cases. Under the catalogue of diffuse glioma, GB is a subtype of astrocytoma. It has been categorised as a Grade IV tumour according to the latest WHO classification (2021) [7], which is the most aggressive malignancy.

Upon historical diagnosis experiences, over 90% of GB are found as the 'primary type'. It is more aggressive and developed directly *de novo* compared to the 'secondary type', which gradually progresses from the low-grade gliomas and is found mainly among younger patients [8][9]. Within clinical practice, the difference between the two types is indistinguishable as they share identical histological characteristics. Nevertheless, alongside the development of technology and understanding of the true nature of the cancers, the genetic profiles are increasingly prioritised for deeper classification.

From the genetic aspect, GB can be robustly categorised according to the mutation status in *IDH 1/2* genes, which play crucial roles in regulating the citric acid cycle in cellular respiration [10]. The primary type can be classified as the '*IDH* wild-type', which describes the unmutated natural state of the genes, while the secondary type frequently shows mutations on the two genes which lead to a changed Krebs cycle product that, instead of reduced nicotinamide adenine

dinucleotide phosphate, a potential oncometabolite 2-hydroxyglutarate is produced [11][12]. A more detailed genomic classification of GB was proposed by the Cancer Genome Atlas Network in 2010 based on signature oncogene abbreviations and expressions: classical, mesenchymal, and proneural, which correlate to epidermal growth factor receptor (EGFR) overexpression and amplification, focal hemizygous deletion of gene *NF1*, and highest focal amplification of platelet-derived growth factor receptor A accompanied with mutated *IDH1*, respectively [13].

Indeed, there are more complex genetic alternations within each case. Genetic characterisation allows early detection of the disease and will contribute to more specific treatment plans for different patients. GB with mutant EGFR is the focus of this thesis and will be addressed in section **1.4**.

1.2.3 GB pathogenesis & treatments

GB is mainly seated in the supratentorial region of cerebral hemispheres; also, a small percentage is found in areas such as the cerebellum, brainstem, and spinal cord. The infiltrative nature of GB allows the diffusive cells to evade brain parenchyma that causes deeper lesions in the thalamus and basal ganglia [14][15], which blocks any possible surgical removal practice. Tumour sites usually exhibit composite features, for example haemorrhage and tissue necrosis are mostly

discovered during histological studies with noticeable morphological changes in the normal brain tissues [16]. Due to the immunosuppressive microenvironment, GB is considered a “cold tumour”, which means the innate immune system can hardly induce T cells to respond to the cancer cells. This contributes to the high recurrence possibility since only exogenous agents lead to some therapeutic success [17][18].

Clinically, patients usually experience symptoms than range from relatively mild such as nausea, headaches and minor neuro-related sensory dysfunction, to severe symptoms such as seizures and unconsciousness. GB is often diagnosed by preliminary neurological exams. Usually, head computed tomography (CT) scan and magnetic resonance imaging (MRI) scan are conducted to locate the lesion sites (Figure 1). Subsequent treatments for GB mainly follow three steps: surgical resection, external beam radiotherapy, and chemotherapy [19] [20].

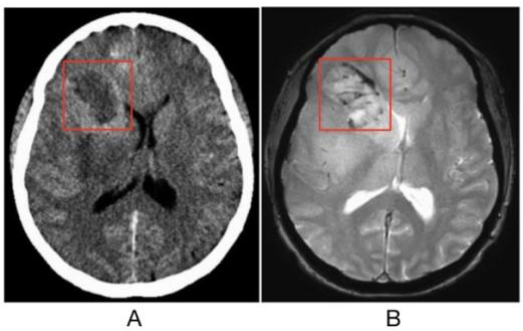


Figure 1: Radiographies of glioblastoma. (A) CT, (B) MRI scans. The tumour is marked with a red square located in the left frontal lobe [21].

However, surgery is not suitable for all patients since the lesion sites might attach to vital brain parts, which also invariably leads to incomplete removal of the tumour sites. Thus, radiotherapy is carried out in both newly diagnosed patients and patients who have undergone surgical excision. It has proven to elevate the post-surgery survival rate by months [22][23]. The dosage of radiation varies from patient to patient based on their Karnofsky performance status, which evaluates the efficacy of the treatment [24]. Elderly patients are usually treated by a method known as “hypofractionation” by increasing daily radiation dosage and reducing total therapy dosage to shorten the treatment course (usually within a few weeks), which helps improve their quality of life [25].

Radiotherapy is always accompanied by chemotherapy for better prognosis results. The agent mostly widely adopted is Temodar® - temozolomide (TMZ), which plays a vital role in clinical treatment as it inhibits GB cell proliferation and contributes to the improved short-term survival rate. As an oral drug, the advised daily dosage ranges from 150 to 200 mg/m^2 (body surface area) for 5 days in a 28-day cycle [26]. In addition, tumour-targeting fields are now utilised as an auxiliary method to enhance the efficacy of the TMZ by placing transducer arrays near the tumour site, then conducting alternating electronic fields with frequencies ranging from 100 to 500 kHz at low intensity, which will disrupt cell division [27]. This combined therapy has been proven to show a significant improvement in survival over drug-taking alone [28].

The developments of different treatments and chemotherapeutic drugs have provided a better prospect in GB prognosis. However, the performance of TMZ is in fact limited my multiple factors and the recurrence of the tumour which shows resistance to the therapeutics remains a challenge [29]. Enhancing the performance of TMZ provides a potential method for optimising post-treatment prognosis.

1.2 Temozolomide

1.2.1 Characteristics

Temozolomide was developed by Malcolm Stevens based on the works of Robert Stones, Ege, and Gilbert in 1980s at Aston University and was approved by the FDA in 1999 as an active therapy in treating recurrent anaplastic astrocytoma, which was later approved for GB first-line therapy and remains a mainstay [30]. Some patients with metastatic melanoma also respond to the drug [31]. The molecular weight of TMZ is 194.15 g/mol. It is stable in acidic solution at pH≤6.0 and quickly decomposes in a neutral or basic environment, with a 1.8-hour plasma half-life (pH 7.2-7.4). The UV-Vis spectrum of TMZ shows two main absorbances: the absorption maxima at 330 nm and a second peak at 257 nm with an extinction coefficient of 7250 $L/mol^{-1}cm^{-1}$. The degradation of TMZ leads to a new peak at 265 nm which stands for the amide group of 4-amino-5-

immidazole-carboxamide (AIC). These characteristics provide a method for detecting TMZ conversion to AIC [32]. The original synthesis was based on the addition reaction of 5-diazo imidazole-4-carboxamide and methyl isocyanate with high yield and product purity (Figure 2). Although many improved alternative synthesis routes were developed, the original route is still used in industrial mass production and appreciated for its 100% atom economic process despite the long reaction time [33].

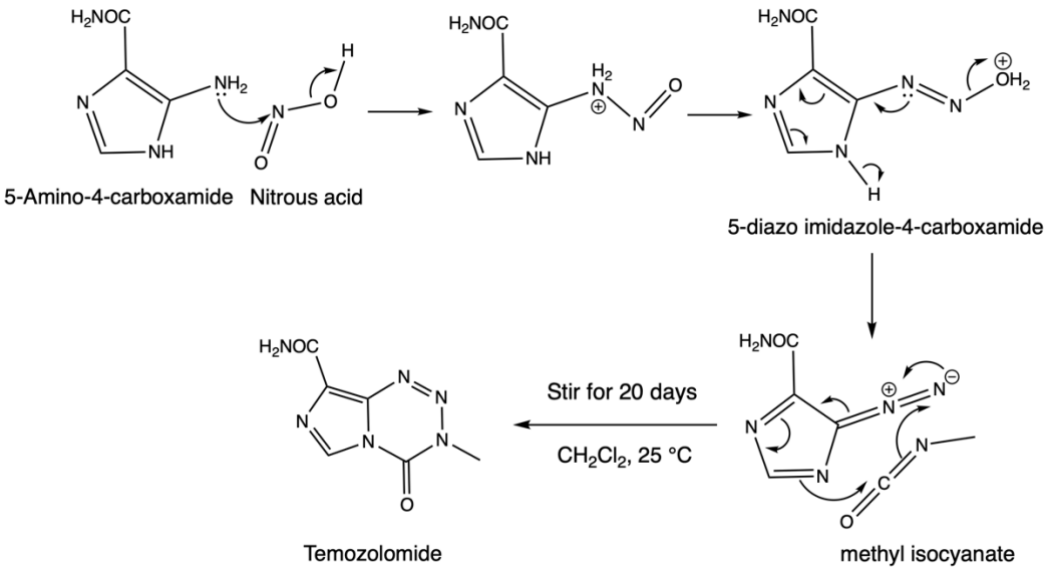


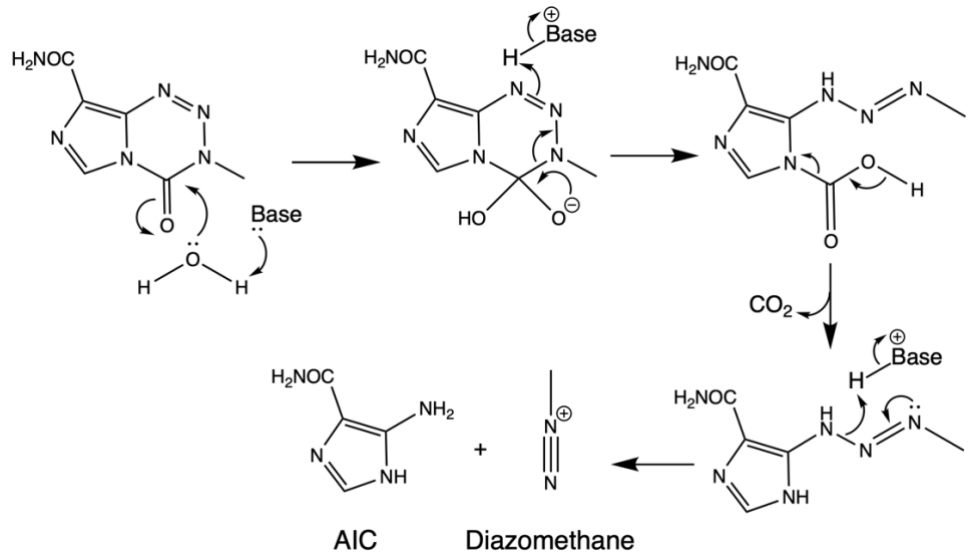
Figure 2: The original synthesis scheme of TMZ. The reaction reaches a yield above 90%.

1.2.2 Mechanism of action

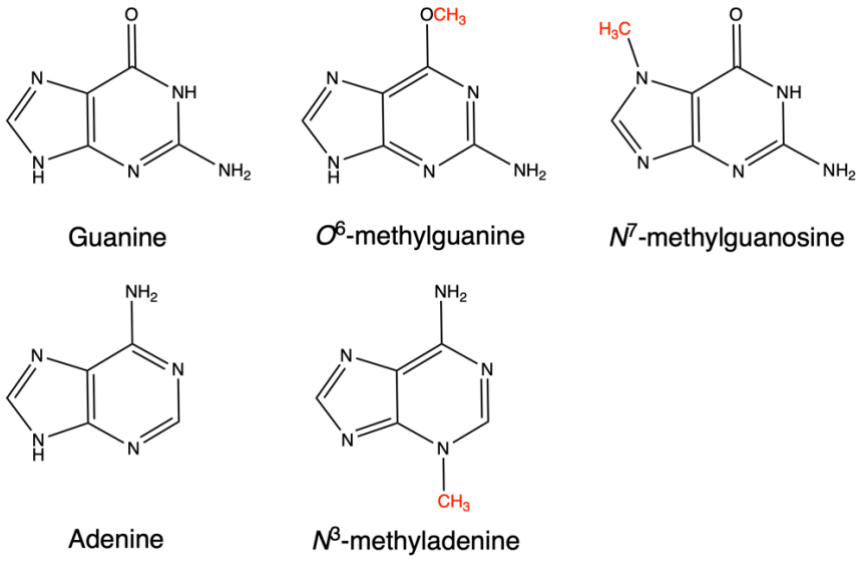
TMZ functions as an antimitotic methylating agent in cancer treatment, which specifically inhibits cell mitosis. After oral intake, the prodrug TMZ is absorbed by the small intestine with 100% bioavailability and is spontaneously hydrolysed in the physiological environment (~pH 7.4) into 3-methyl-(triazen-1-yl) imidazole-4-carboximide (MTIC). MTIC is then further degraded into a biologically inactive metabolite AIC and potent alkylating agent diazomethane (Figure 3: A) [34][35]. All metabolic products are excreted through the kidneys, which also limits the given dosage to ease the burden on the urinary system. Diazomethane that enters the nucleus of GB cells methylates the DNA nucleobases during the S phase in cell cycle, and the main products are N^7-methylguanosine (*N*7-MeG), N^3-methyladenine (*N*3-MeA), and O^6-methylguanine (*O*6-MeG) (Figure 3: B) [33][36].

As the majority of *N*7-MeG and *N*3-MeA modified bases are corrected by a base excision repair mechanism, the antimitotic activity relies on the mismatch of *O*6-MeG [37]. Instead of cytosine, *O*6-MeG mispairs with thymine; hence the DNA mismatch repair mechanism (MMR) is triggered to substitute the thymine of the daughter strand with a corrected pairing base for *O*6-MeG which does not exist, and thymine is re-inserted. The futile cycle of mismatching and excision eventually causes the accumulation of nicks and leads to the breakdown of the

DNA replication fork (Figure 4); hence the cell fails to cross the G_2/M checkpoint, and apoptotic or autophagic cell death is activated [38][39].



(A)



(B)

Figure 3: (A) Mechanism of TMZ hydrolysis into MTIC, (B) Natural nucleobases and their methylation derivatives. The added methyl group is marked in red N3-methyl, N7-methyl, O6-methyl.

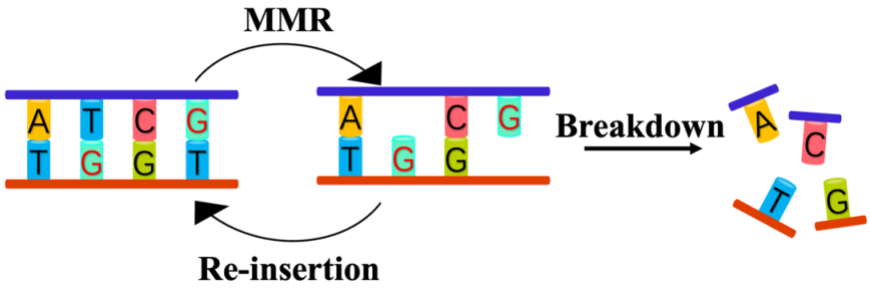


Figure 4: Mechanism of MMR-involved DNA-mismatching cycle. A, G, C, T represent adenine, guanine, cytosine and thymine, respectively. The red-highlighted G represents *O*6-MeG.

1.2.3 Challenges

1.2.3.1 Toxicity

Although TMZ has been actively adopted as the chemotherapy choice for GB, its performance is limited by multiple factors in clinical practice. Clinically, GB requires frequent and scheduled exposure to TMZ to prevent tumour progression; however, as an antimitotic drug, it fails to distinguish normal cells from cancer cells in inhibiting cell growth. It has been shown that TMZ has a potential risk of inducing haematologic toxicity which causes damages to the immune system, such as myelosuppression and thrombocytopenia, which are reported at a 15~20% occurrence rate [40]. This leads to not only TMZ dosage limitation, but also disruption or even termination of the treatment cycle as it might result in patients experiencing dangerous infections, which eventually contributes to poor prognosis.

1.2.3.2 Blood brain barrier (BBB)

As the most crucial part of the human body, the brain blood vessels serve a vital role in regulating and protecting the CNS. The cerebral capillaries are comprised of a unique endothelial cell phenotype which strictly governs the substance exchange to prevent the invasion of any toxins. This synergy between the brain capillaries and the surrounding microenvironment that maintains brain homeostasis is known as the blood brain barrier (BBB) [41] [42]. However, this defense mechanism also restricts the entrance of therapeutic drugs. Even though TMZ is of small molecular size and weight which allow it to diffuse through BBB, the number of molecules that successfully penetrate the lesion site is not ideal. A pharmacokinetic study has discovered a mean peak concentration of only 0.3~0.9 μg/mL in the brain after 2 h of 75 mg administration, which is only 17.8% of the concentration found in plasma [43].

1.2.3.3 *O*^{6}-Methylguanine-DNA methyltransferase (MGMT)

As mentioned in the previous paragraph, the actively functioning MMR mechanism contributes to the cytotoxicity of TMZ treatment. However, it is not applicable to every GB subtypes. MGMT is a direct DNA repair enzyme that precisely removes the methyl group from *O*6-MeG and restores the DNA replication, hence “rescues” the cell from paused cell cycle and apoptosis. The detection of MGMT level is conducted by monitoring the methylation status of

the MGMT promoter, indicating epigenetic gene silencing [44]. Thus, the patients with a low level of MGMT promotor methylation often show resistance to TMZ. Moreover, the patients who received alkylating agent treatment tend to show an active MGMT expression in their recurrent tumour cells generated from the "survivors" of previous treatment [37][45]. Therefore, suppressing the MGMT repairing mechanism provides a way to eliminate cancer cells and reduce recurrence possibility. It can be deduced that since the MGMT mechanism requires a minimum of one molecule for each *O*6-MeG [46], a localised high concentration of TMZ will create higher number of DNA adducts, thus outnumbering the 'resistance' repairing mechanism. Due to the dosage limitation, this requires a targeted method of transporting TMZ into the tumour sites to conquer the obstacles mentioned above. The method itself needs to be biocompatible and able to pass through the BBB. From the investigation into the abundance of receptors of BBB capillary endothelial cells, and the brain's needs for iron, the possibility of utilizing (apo)ferritin that is transcytosed across the BBB using the transferrin receptor TfR1 emerge [47][48].

1.3 Apoferritin

1.3.1 Background & Characteristics

Ferritin is an essential iron storage protein ubiquitously found in both eukaryotes and prokaryotes. The protein component without iron is called apoferritin (AFt).

There are three types of AFt: the classical type; bacterioferritin which contains heam groups; and DNA-binding protein from the starved cells [49]. The classical type which plays a dominant role in the natural world is the focus of our research, as the other two types are from prokaryotic sources, which are not ideal for clinical applications as they are likely to elicit a strong immune response. Currently, human AFt and horse spleen AFt are the most common types being used in drug delivery research.

AFt is a hollow sphere with a 12 nm outer diameter and 8 nm diameter interior cavity (Figure 5). It is constituted of 24 subunits with negative charges of two types: the heavy (H) chain (21 kDa) and the light (L) chain (19 kDa), and the ratio of the two subunits varies in different tissues [50]. The ferroxidase centre in the H subunit performs the oxidation of Fe^{2+}, while the activity of the L subunit is related to the biomineralisation of Fe^{3+} into an iron hydroxide core up to 4500 iron ions [51], protecting cells from Fenton reaction oxidation damage. The subunits junctions form in total six 4-fold hydrophobic and eight 3-fold hydrophilic pores (~0.3 nm) on the protein surface, which allows the entrance of various small molecules including iron ions [52].

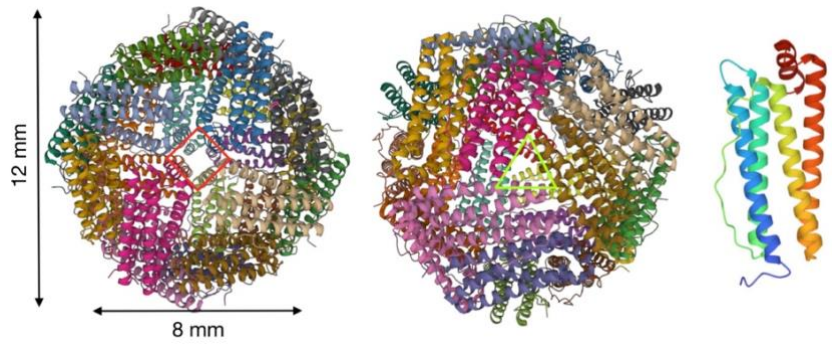


Figure 5: 3D structure of recombinant human heavy chain AFt and heavy chain subunit. 3-fold and 4-fold pores are marked. Image obtained from PDB, ID:7VD8.

The structure of AFt is remarkably stable chemically and thermally. It can tolerate temperatures up to 85 ℃ and 6 M urea at pH 7.0 [53] and has been reported to have an excellent long-term (12 weeks) stability in water at 4 ℃ [54]. An intact structure is retained over a pH range of 3.4-10.0 in aqueous solution. AFt gradually disassembles outside this range but can be restored to its original structure when the pH is adjusted back within this range [55]. These combined structural properties offer vast potential for utilising AFt as a drug-loaded nano-cage.

1.3.2 Biocompatible nano-cage

There are two main methods for drug-loading. The first one is by passive diffusion, small drug molecules (smaller than sucrose) enter the cavity *via* the surface pores; the second one is by chemical disassembly-reassembly of subunits to capture larger molecules (Figure 6). These methods have been demonstrated to

successfully encapsulate a wide range of drug molecules and even small proteins and inorganic quantum dots [56][57].

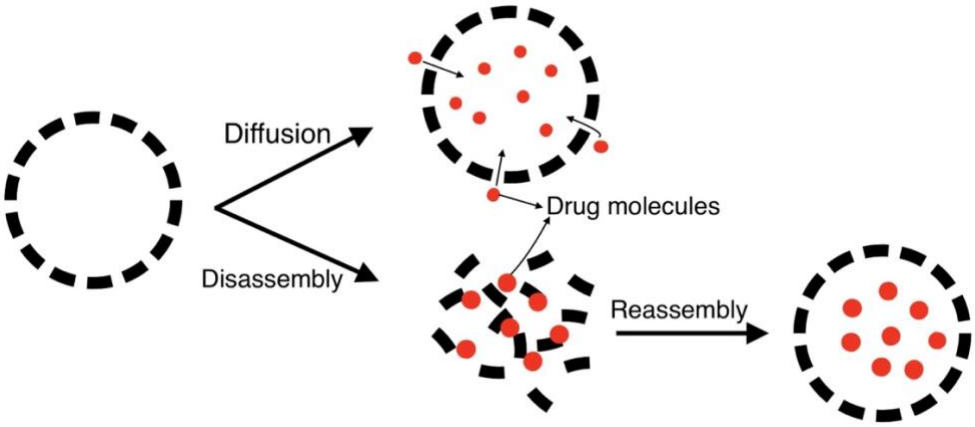


Figure 6: The two schemes of drug-encapsulation.

Due to the universal iron-transportation/storage demands in almost all cell types, the transferrin receptor 1 (TfR1) is a common receptor for the iron-transportation protein transferrin and widely found in many types of cancer cells, including GB and BBB endothelial cells where it is found at high levels. AFt also benefits from TfR1-mediated transportation across the cytoplasmic membrane. Natural AFt can bind and be recognised on the H chain by TfR1 and enters the cells *via* endocytosis, then accumulated in the early endosomes. The iron ions are released in acidic late endosomes and lysosomes environment from enzyme-driven disassembly of AFt under pH 4.9-6.0. It has been reported that the recombinant human H-AFt (only comprised of heavy chain subunits) is able to translocate into cell nucleus due to its potent “endosome escape” ability which prevents its entering into late endosomes and lysosome [58][59].

Therefore, in recent years AFt has been adopted for multiple purposes including drug delivery and medical imaging, available both *in vivo* and *in vitro*. [60]. Moreover, the 24 N-termini are distributed around the 3-fold pores and extended outside the protein surface, and the 24 C-termini are partially buried at the 4-fold pores unless modified with reasonably large peptides in which case they emerge from the exterior. Together these offer 48 positionally defined modification sites for more specific biomarker/receptor-targeting functionalisation [52][61]. In the case of GB, the EGFR family of cytoplasmic membrane spanning proteins is a validated biomarker as these are overexpressed.

1.4 EGFR: a biomarker of GB

1.4.1 Receptor tyrosine kinases

Receptor tyrosine kinases (RTKs) are single-pass transmembrane receptors that dominate the signal cascade *via* enzymatic reactions. They play important roles in regulating cell proliferation, differentiation, motility, survival and many other activities. The overall structures of whole RTK families share high-level similarities, that all are composed of five structural parts: the extracellular domain (EC) that binds to the regulator peptides; the transmembrane helix region (TM); the cytoplasmic domain where the tyrosine kinases are located at (TKD); a carboxy-terminal tail region (C terminal); and the juxtamembrane region (JM), which is a short amino acid sequence composed of 40 to 80 residues, connecting

the TM and TKD (Figure 7). Currently, 58 types of RTKs have been found in the human body and can be further subcategorised into 20 different families such as EGFRs and fibroblast growth factor receptors (FGFRs) according to their extracellular region structures [62][63].

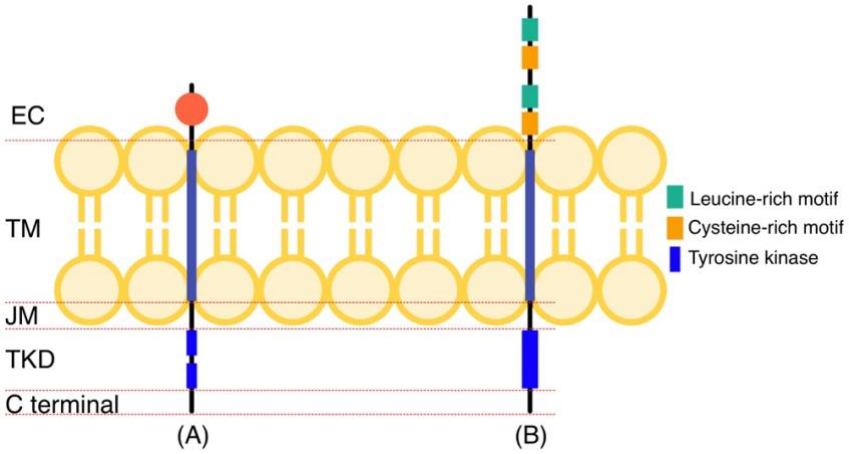


Figure 7: RTKs structure (A) General structure of RTKs, the extracellular red circle represents different functional domains and motifs; (B) Structure of EGFRs family.

Predominantly, when no binding ligand is present, the RTKs on the cell surface remain in an autoinhibited state. Most RTKs stay in monomeric form when inactivated, while some RTK subsets occur as disulfide-linked dimers. The enzymatic activity of RTKs usually is activated through dimerization or oligomerisation. The overall synergy across each region in signal transduction remains undiscovered due to the limitation on full-structure RTK extraction, that function of each region is only understood as individual component [64]. Nevertheless, the general mechanism of RTK activation is well studied, and the binding ligands serve important roles in the RTK activation. Upon recognition of

the regulators or by regulator cross-link, the conformation of the EC of inactivated receptors changes enabling the binding domains of nearby receptors to contact each other, thus reaching the dimeric state. The existence of ligands also helps stabilise dimer formation. The TKD is hence activated and trans-phosphorylates the nearby RTKs to increase the localised activated TKD concentration to promote multiple downstream signaling pathways [62][65]. Other regions are also functionally involved in the activation mechanism: The JM helps maintain the autoinhibition state, while a stable TM conformation is tightly related to successful signal transduction [66][67].

1.4.2 EGFR family (EGFRs)

As mentioned in the previous chapter, genetic alteration is an essential factor in characterising cancer subtypes. EGFR plays a crucial role in epithelial development, which impacts many physiological activities such as homeostasis and organ generations [68]. However, among all types of GB, around 60% shows overexpression of EGFR, and around 40% exhibits amplification of oncogene *EGFR.* EGFR dysfunction is also found in many other malignancies, which usually indicates promoted metastasis and proliferation abilities of the disease and a poor prognosis [69][70].

The EGFR family (Figure 7), also known as ErbB or HER family, consists of 4 structurally related RTKs: EGFR (ErbB1/HER1), HER2 (ErbB2), HER3 (ErbB3), and HER4 (ErbB4). In the EC region the two leucine-rich motifs (domains 1 and 3) are the regulator-binding sites, and the dimerisation site on the cysteine-rich motif domain 2 is occluded, while domain 4 tethers domain 2 to stabilise the conformation. EGFRs bind to eleven different growth factors, which are categorised into four groups (Figure 8) [68]. For the majority, a ligand binds to a single EGFR and discloses the dimerisation site to the nearby deformed EC, hence triggering dimerisation and kinase activation. Dimerisation also occurs without the presence of regulators. Around 10% of the total EGFR population are naturally present as dimers and the activation of the TKD is also induced by binding with two ligands (Figure 9) [71]. Homo- or heterodimerisation are both feasible, and overexpression of certain phenotype will lead to prevalent homodimerisation [72]. By binding signaling proteins such as Src homology 2 and phosphotyrosine binding proteins, the dimerization activates TKDs by "activator" TDK C-lobe direct contact with "receiver" TDK N-lobe, and the downstream pathways are triggered, including RAS/MAPK, PI3K/AKT and PI3-kinase pathways which regulate the cell growth and proliferation as well as survival [73].

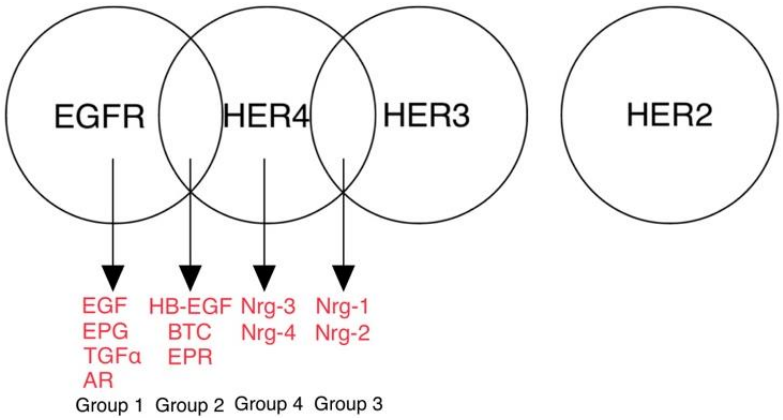


Figure 8: Recognition of 14 growth factors. The crossover section indicates the group recognises both types. It is notable that HER2 does not have known ligands. (EPG: epigen, AR: amphiregulin, TGF: transforming growth factor, BTC: betacellulin, EPR: epiregulin, Nrg: neuregulin)

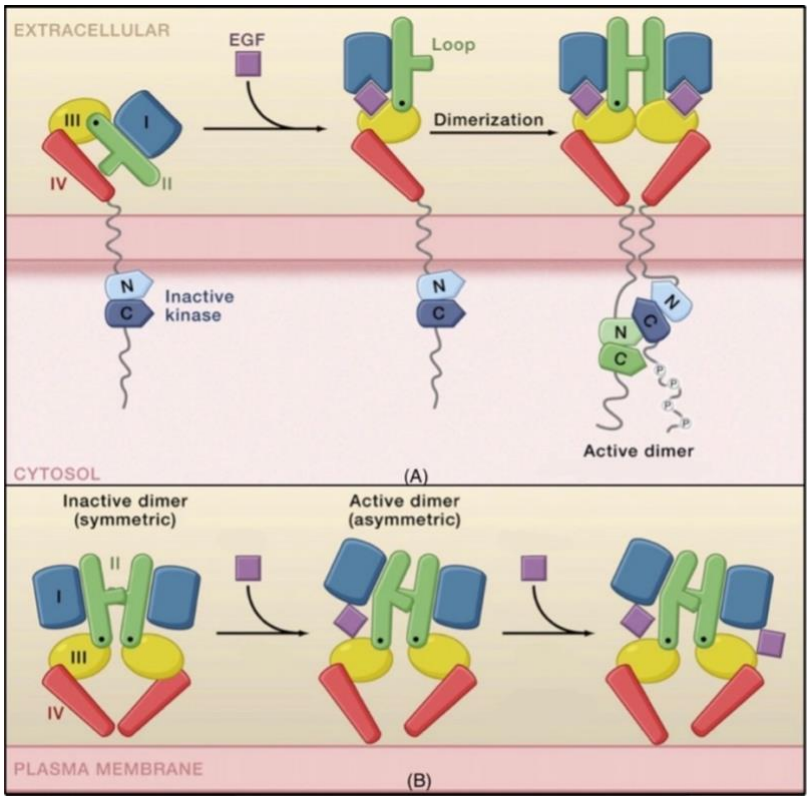


Figure 9: The EGFRs dimerisation schemes [74]. (A) Upon recognition of ligand, two nearby EGFR dimerise by exposing and contacting their dimerisation arms (II), hence activate the kinases; **(B)** For innate dimer, the two regulator-bindings are almost simultaneous, with a dimerisation arm bended by the first binding. The TKD is therefore activated as shown in (A).

Although EGFR overexpression often means poor treatment outcome upon clinical diagnosis, it does provide a unique cellular surface characteristic for targeted treatment. Moreover, EGFR is regulated by “receptor trafficking” in an internalisation-release cycle, where the activated EGFR dimers are endocytosed and released back to the cellular surface by endosomes, while a portion is degraded by lysosomes. Ligand-binding notably accelerates this process [75][76]. This allows the modified anti-EGFR agents to enter and be released intracellularly, which satisfyingly fits the idea of GB-targeted AFt transportation. To maintain the innate structure of AFt for the best biocompatibility of the protein, a small binding moiety should be considered and fused on the cage surface for the targeting purpose, and the development of affibodies meets this demand.

1.5 Affibody modified AFt: promising targeting drug delivery system

1.5.1 Background

Since their discovery in the 1990s, affibodies have become successful affinity molecules for many therapeutic research fields. The fundamental development of affibodies was carried out by separating a 58-amino acid peptide from the engineered Ig-binding region of staphylococcal protein A (SPA). The 3-helix peptide obtained still maintained a partial affinity compared to SPA and is called a Z-domain scaffold (Figure 10) [77][78]. Affibodies are usually selected by the

phage display method. A “library” of phages with Z-domain scaffolds fused to their coat protein containing any of the proteinogenic amino acids at 13 positions on helices 1 and 2 are washed over different affinity targets, and by multiple cycles of this selection, affibodies are picked out with different specificity and affinity levels [79]. Affibodies possess advantages including their small yet robust molecular structure, with a molecular weight of around 6500 Da. Compared to traditional multi-domain monoclonal antibodies which contain disulfide bonds that makes their economic production difficult, the short sequence also grants affibodies compact intermolecular interactions as α-helix, which promotes their strong stability. Other than the structural advantages, affibodies also benefit from their economic production method (bacteria expression), minimal background interference, and simple functioning mechanism [80][81]. After years of development, multiple affibodies of various sequences for EGFR/HER RTK family are already available for research purposes and have been incorporated in multiple nanotherapeutics studies because of their exceptional affinity characteristics; for example, HER2 affibody-labelled radioisotopes have potential application for *in vivo* breast cancer imaging in which HER2 overexpression is often observed [82]; the HER3 affibody was shown to compete with the natural regulator in ligand-binding and shows a suppression on TDK activation [83].



Figure 10: General structure of the 3 α-helix Z-domain scaffold. Image obtained from PDB, ID: 2B89.

1.5.2 EGFR affibody-AFt fusion protein

Existing research has developed a specific prostate membrane antibody-AFt fusion to encapsulate doxorubicin, which is a potent anti-cancer drug. Although the targeted delivery system was only of equivalent *in vitro* cytotoxicity with non-targeted Aft delivery system, it showed a selectivity with a decreased toxicity towards normal endothelial cells comparing to both free drug molecules and a non-targeted system. An additional haemocompatibility of the targeted system was also demonstrated with potential *in vivo* application [84]. An AFt-encapsulated TMZ system has shown significantly enhanced *in vitro* activity compared to free TMZ in two U373 isogenic GB cell lines transfected with MGMT or empty vector [85]. Based on these findings, an EGFR-affibody-AFt fusion TMZ delivery system is anticipated to show an enhanced effectiveness in GB treatment.

Several EGFR-affibodies have been developed and made available for research work; for example, $Z_{EGFR:1907}$ has been investigated as a radionuclide imaging agent, while $Z_{EGFR:2377}$ was tested in murine xenografts as an EGFR expression indicator (Figure 11) [86][87]. $Z_{EGFR:2377}$ was reported to have an ideal equilibrium dissociation constant (K_D) value of 160 pM, indicating a high sensitivity to its antigen [88].

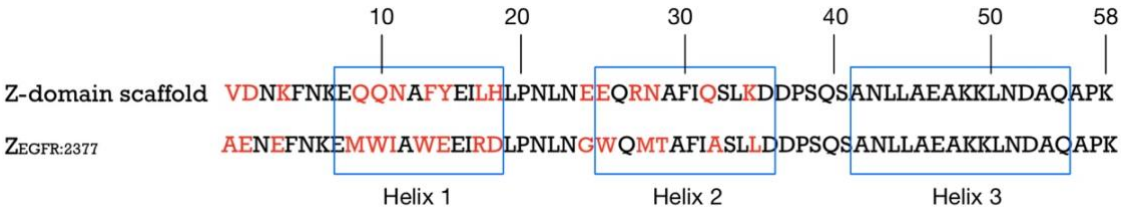


Figure 11: Sequences of Z-domain scaffold and $Z_{EGFR:2377}$. The three helices are marked with blue squares, and the amino acid alterations are highlighted in red.

In our research group, Dr Lei Zhang and PhD student Isobel Holden have successfully developed the plasmids and constructed lab-based bacteria expression systems for $Z_{EGFR:2377}$ affibody of 8464 Da and a 24 affibody-human H chain AFt fusion at N-terminals (EGFRa@AFt), also the human H-AFt of 584 kDa. Each of these recombinant proteins were designed with 6 x His-tags® for nickel-affinity purification. The modified recombinant EGFRa@AFt shows preserved chemical and physical characteristics, with a MW of 732 kDa (Figure 12).

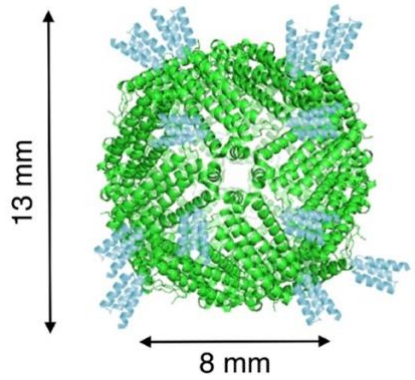


Figure 12: 3D structure of EGFRa@AFt. Plain-side view shows 12 affibodies fused on the protein surface. Image was created by Isobel Holden.

2. Objectives

The purpose of this study was based on the research previously carried out by Dr Lei Zhang, Isobel Holden and Dr Kauthar Bouzinab [85], using EGFRa@AFt as a nanocage to construct a GB-targeting drug delivery system of TMZ by:

- Utilising an *E. coli* protein expression system to produce the recombinant proteins human H-AFt, EGFRa@AFt and EGFR-affibody. Their purities and reassembly properties being determined by electrophoresis.
- Verifying the stability of TMZ and structural integrities of proteins under encapsulation conditions and finding out suitable storage conditions for encapsulated drugs.
- Encapsulating TMZ with both EGFRa@AFt (EGFRa@AFt-TMZ) and human H-AFt (AFt-TMZ), verifying the diffusion-encapsulation mechanism *via* fluorescent TMZ molecule mimetic.
- Testing the growth-inhibitory effectiveness of EGFRa@AFt-TMZ *via* mammalian cell assays and in parallel comparing with AFt-TMZ and free TMZ molecules.
- Examining the EGFR receptor expression status of the chosen cell lines by Western blot.

3. Methods

3.1 Materials

3.1.1 Chemical substances

Material	Suppliers
EDTA-free protease inhibitor	Merck
Dimethyl sulfoxide (DMSO)	Thermo Fisher
Glycine	Merck
Methanol (99.8% v/v)	Merck
Neutral red	Alfa Aesar
Sodium chloride	Thermo Fisher
Trizma base (tris)	Merck

Table 1. General materials. The materials (except for neutral red) above were utlised in multiple experiment processes.

Material	Suppliers
Carbenicillin	Merck
Ethylenediaminetetraacetic acid (EDTA)	Merck
Imidazole	Merck
Isopropyl β-D-1-thiogalactopyranoside (IPTG, 1 M)	Merck
Lysogeny broth (LB) broth with agar	Merck
Super optimal broth with catabolite repression (S.O.C.) medium	Thermo Fisher

Table 2. Protein production materials. S.O.C. medium was sterile upon purchase. IPTG was sterilised by 0.22 μm filter.

Material	Suppliers
Acrylamide mix solution (30% v/v)	Merck
Ammonium persulfate	Bio-Rad
Bromophenol blue	Merck
Coomassie blue	Bio-Rad
Dithiothreitol (DTT)	Merck
Glycerol	Merck
Isopropanol	Thermo Fisher
Glycerol	Merck
N, N, N′, N′-Tetramethyl ethylenediamine (TEMED)	Merck
Pre-stained protein ladder	Thermo Fisher
Unstained low-range protein ladder	Thermo Fisher
Unstained native PAGE mark	Thermo Fisher
Sodium dodecyl-sulfate	Merck
Xylene cyanol	Merck

Table 3. Electrophoresis materials.

Antibody	supplier
EGFR Recombinant Rabbit Monoclonal Antibody	Merck
Goat anti-Rabbit IgG (H+L) Secondary Antibody (HRP-conjugated)	Thermo Fisher
Material	**supplier**
Bovine Serum Albumin	Bio-Rad
Bradford reagent	Bio-Rad
Enhanced chemiluminescence (ECL) reagent	Amersham
RIPA lysis buffer 10X	Thermo Fisher
Skimmed milk powder	Sainsbury's
Tween 20	Merck

Table 4. Western blot materials.

Medium	**Suppliers**
Eagle's minimal essential medium	Merck
RPMI-1640 medium	Merck
Material	
3-(4,5-dimethylthiazol-2-yl)-2,5-diphenyltetrazolium bromide (MTT)	Invitrogen
Fetal bovine serum	Merck
G418 Sulfate (50 mg/mL)	Corning
Gentamicin solution [50 mg/mL in deionized water (dH_2O)]	Merck
L-glutamine (200 mM solution)	Corning
MEM non-essential amino acid 100X (NEAA)	Merck
Methylene blue	Merck
Penicillin/streptomycin 50X (pen/strep)	Corning
Phosphate-buffered saline (PBS)	Merck
Phosphatase inhibitor	Roche
Radioimmunoprecipitation assay (RIPA) buffer 10X	Merck
Trypsin solution 10X	Merck

Table 5. Mammalian cell experiments materials. All materials were sterile during experiments.

3.1.2 DNA plasmids

Plasmids of EGFRa@AFt, human H-AFt and EGFR-affibody were designed by Isobel Holden and were stored at -20 ℃ (Figure 13).

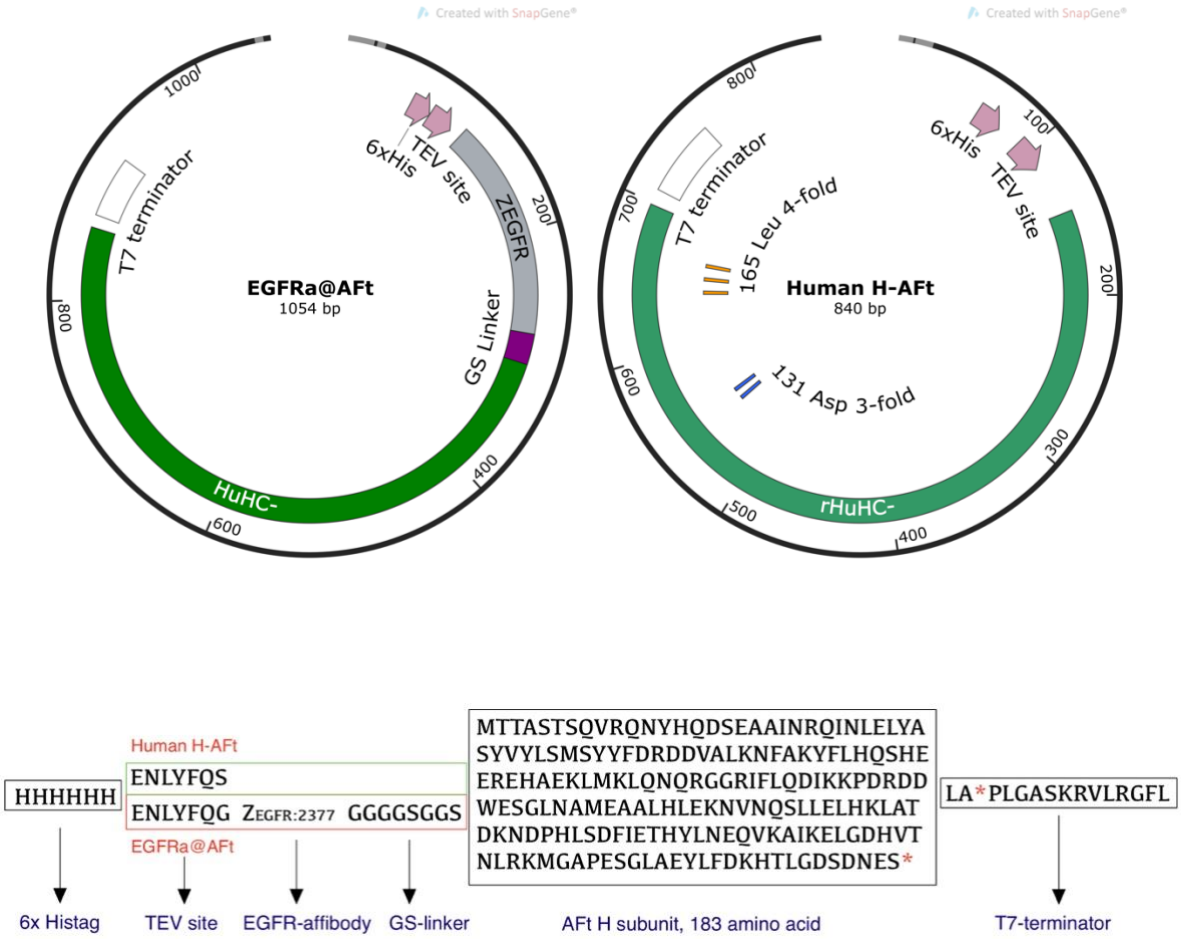


Figure 13: Plasmid maps and amino acid sequences of human H-AFt and EGFRa@AFt subunits. TEV site stands for the Tobacco Etch Virus (TEV) protease cleavage site for Histags; GS linker helps improve the protein stability; red * stands for stop codon. Plasmid images generated by SnapGene software.

3.1.3 Cell lines & growth medium

The cells of choice for MTT viability assay and clonogenic assay were:

- **Human glioblastoma U373V** (vector control; EGFR-overexpressed) and **isogenic U373M** (MGMT-transfected; EGFR-overexpressed, MGMT+).
- **Human colon carcinoma HCT-116** (EGFR-overexpressed, MGMT+, MMR deficient).
- **Human fetal lung fibroblast MRC-5** (non-tumourigenic control).

Recipes of nutrient growth medium for each cell line are listed below:

- **U373V/M:** PMI-1640 medium with 10% (v/v) FBS, 1% (v/v) NEAA, 0.03% (w/v) L-glutamine, 0.02% (w/v) G418, 0.03% (w/v) gentamicin.
- **MRC-5:** Eagle's minimal essential medium with 10% (v/v) FBS, 1% (v/v) NEAA, 0.01% (w/v) pen/strep, 0.03% (w/v) L-glutamine.
- **HCT-116:** RPMI-1640 medium with 10% (v/v) FBS and 0.01% (w/v) pen/strep.

Cells were purchased from ATCC and stored in the cell bank (liquid N2). All procedures involving cell lines were carried out under strict aseptic conditions in a BIOMAT2® Microbiological Class 2 Safety Cabinet and all apparatus was sterilised with 70% v/v industrial methylated spirit (IMS). Growth media were consumed within 2 months.

3.2 Protein expression in *E. coli*

3.2.1 Transformation

All microbiological experiments were carried out in a sterile environment alongside all growth media and apparatus being autoclaved at 120 ℃ for 26 min before use. Tuner^{TM} *E. coli* strain (Sigma) were chosen for plasmid transformation (stored at -80 ℃). The cells were thawed for 5 min and then 1 μL of plasmid (100-200 ng/μL) was added to the cell suspension. The mixture underwent “heat-shock" at 42 ℃ for 30 s and then cooled on ice for 5 min. Once the time had elapsed 950 μL of warmed S.O.C. medium was added for recovery and the *E. coli* suspension was incubated at 37 ℃, with orbital shaking (200 RPM) for 1 h. The transformed cell suspension (20 μL) was streaked onto an agar plate with an inoculation loop, and the plate was incubated under 37 ℃ for 16 - 18 h for colony formation with carbenicillin as a selection marker. Following bacterial colony growth, the agar plates were stored at 4℃ for up to two weeks.

3.2.2 *E. coli* culture

E. coli culture took place in LB medium [2.5% w/v LB broth in ultra-pure dH_2O (milli-Q water), 50 μg/mL carbenicillin]. A single bacteria colony was added into 10 mL LB media, then incubated at 37 ℃ and shaken at 200 RPM for 16-18 h. The 10 mL cell culture was used to inoculate a 1 L LB medium then incubated at

37 ℃ and shaken at 200 RPM until it had reached an OD600 value between 0.6 - 0.9. Once the 1 L culture had reached the appropriate OD, 50 µL of IPTG was added into the 1 L culture (50 µM) to induce protein expression. The culture was further incubated at 18 ℃, shaking at 200 RPM for 16-18 h. The cell culture was pelleted *via* centrifugation at 4000 g, 4 ℃ for 20 min. The excess media was discarded, while the obtained pellets were suspended in 40 mL of elution buffer A (**3.2.4**) and flash frozen for storage at -80 ℃.

3.2.3 Protein extraction

Protease inhibitor (1 tablet) was added prior to the thawing of the cell pellet. Once the cell pellet was defrosted, the suspension was sonicated for 10 min (1 min on/ 1 min off). The lysed cell pellet was centrifuged at 35,000 g, 4 ℃ for 30 min. At this stage, for EGFR-affibody extraction, all affibodies were collected in the supernatant. For both AFts, the supernatant was discarded and the insoluble pellets were dissolved in 20 mL of insoluble buffer (20 mM tris, 4 M urea, pH 9.0). The solution was again centrifuged at 35,000 g, 4 ℃ for 30 min. The proteins were collected in the new soluble fraction (supernatant) and the insoluble pellet was discarded.

The EGFR-affibody soluble fraction was dialysed in dialysis buffer (20 mM tris, pH 9.0, MWCO 3500 Da dialysis membrane) overnight and ready for

purification. Before taken forward for affinity purification, both AFts extractions were dialysed (MWCO 6-8000 Da dialysis membrane) firstly with an additional 0.05 M of EDTA. On the next day, the dialysis tubing was transferred to fresh dialysis buffer for 24 h. The buffer was refreshed after 10 h. Dialysis was conducted at 4 ℃ with constant rotation.

3.2.4 Sample purification

The purification was carried out by ÄKTA™ prime chromatography system at a pressure limit of 0.5 MPa, and a maximum column-loading rate at 5 mL/min. All buffers used were pre-degassed and sterilised through a 0.22 μm cellulose filter. The recipes for elution buffers are listed in the table below:

Buffer	Substances (mM)			pH
	Tris	Imidazole	NaCl	
A	20	30	100	9
B	20	700	100	9
A_2	20		50	11
B_2	20		1000	11

Table 6: Recipes for elution buffers.

3.2.4.1 Immobilised metal affinity chromatography (Nickel)

The protein extractions were filtered with 0.22 μm cellulose filter. The Hitrap™ chelating HP column was charged with 1 M degassed $NiSO_4$. The column was washed with buffer A and the soluble fractions were then loaded onto the column with sequential dilution with buffer A until the absorbance reading dropped under 0.03 AU. During the loading, the flow-through was collected. For human H-AFt and EGFRa@AFt, the column was eluted with 10%, 20%, 70% and 100% of buffer B (v/v in buffer A); and for EGFR-affibody was eluted with 2%, 5%, 8%, 10% and 100% of buffer B (v/v in buffer A).

The collected fractions which contained proteins of interest based on the SDS PAGE results were dialysed overnight (see **3.3**). After dialysis, the EGFR-affibody sample was concentrated using spin filters (MWCO 3000 Da) by multiple centrifugations at 4000 g, 4 ℃ for 30 min until the concentration reached to > 2 mg/mL. The concentrated sample was aliquoted and flash frozen, stored at -80℃.

3.2.4.2 Anion exchange chromatography (anion exchange)

For both AFts, the pH of the dialysed samples was adjusted to 12 with 1 M NaOH. The purification procedure was same as **3.2.4.1**. The HiTrap™ Q HP column was loaded with buffer A_2. After sample was all loaded, the column was eluted with 10%, 20%, 40%, 50%, 60%, 100% of buffer B_2 (v/v in buffer A_2). The fractions contained proteins of interest were dialysed in dialysis buffer overnight. As in **3.2.4.1**, the protein samples were concentrated (MWCO 30000 Da spin filter) and stored.

3.3 Electrophoresis

3.3.1 Gel preparation

The sodium dodecyl-sulfate (SDS) gel used was comprised of 5% stacking gel and 15% resolving gel, while the native gel was of 4% stacking and 6% resolving. The recipes of the gels are shown in Table 7.

	SDS PAGE		Native PAGE	
	Stacking gel (5%)	Resolving gel (15%)	Stacking gel (4%)	Resolving gel (6%)
10% (w/v) SDS	50 µL	100 µL		
1.0 M Tris (pH 6.8)	0.63 mL		0.94 mL	
1.6 M Tris (pH 8.8)		2.50 mL		3 mL
Milli-Q H_2O	3.40 mL	2.30 mL	2.88 mL	6.66 mL
Acrylamide mix solution (30%)	0.83 mL	5 mL	0.50 mL	2.30 mL
10% (w/v) Ammonium persulfate	50 µL	100 µL	60 µL	150 µL
TEMED	5 µL	4 µL	6 µL	15 µL

Table 7: Recipes for SDS PAGE and native PAGE gels.

Both SDS and native PAGE gels were prepared in the Bio-rad™ gel casters. After the resolving gel was mixed with TEMED and pipetted into the glass molds, and isopropanol (70% v/v, 100 µL) was distributed evenly on the top to level the gel surface. After the resolving gel polymerised (20-30 min), isopropanol was removed, and the stacking gel was layered on the top of the resolving part. Comb of 10 or 15 wells was inserted in stacking gel and was allowed to polymerise for 20-30 min. The gel was soaked in milli-Q water and stored at 4 ℃ for at least 18 h before use for complete matrix polymerisation and were used within 1 week.

3.3.2 Performing electrophoresis

Electrophoresis was conducted in Bio-rad™ Mini-PROTEAN® electrophoresis system. The recipes for 10X running buffer and 4X loading dye are listed below:

Substances	SDS PAGE	Native PAGE
Glycine	14% (w/v)	15% (w/v)
Tris	3% (w/v)	3% (w/v)
SDS	1% (w/v)	

Table 8: Recipes for 10X running buffer (in dH_2O).

Substances	SDS PAGE	Native PAGE
Xylene cyanol		0.25 (w/v)
Glycerol	32% (v/v)	50% (v/v)
Bromophenol blue	0.4% (w/v)	0.1% (w/v)
1 M Tris buffer (pH 6.5)	20% (v/v)	
SDS	8% (w/v)	
DTT	40% (v/v)	

Table 9: Recipes for 4X loading dye (in milli-Q water).

Samples (12 µL) were mixed with 4 µL loading dye. The loading samples for SDS PAGE were heated for 5 min at 90 ℃. The gel was fully submerged in 1X running buffer (10X running buffer diluted with dH_2O in 10% v/v).

Subsequently, 5 µL unstained low-range protein ladder (SDS PAGE, Thermo

Fisher) or native marker (native PAGE, Thermo Fisher) was added to the well followed by 10 μL of each loading sample. For SDS PAGE, electrophoresis was carried out at 180 V for 10 min then increased to 200 V for another 40 min; For native PAGE electrophoresis was at 100 V for 2.5 h. The gels were then washed by microwaving in water for 1 min, 3 times and stained by microwaving in Coomassie blue for 2 min, then washed again. The stained gels were submerged in water and shaken at 200 RPM overnight before imaging, while the gels indicating affibodies were imaged right away as they diffused rapidly from the matrix due to their low MW.

3.4 Investigating TMZ stability

TMZ powder (0.0097 g, gifted by Dr Bouzinab) was dissolved in 2 mL of DMSO to prepare 25 mM TMZ DMSO sample. Subsequently it was further diluted into 3 tris buffers (20 mM; pH 3.5, 6.5, 8.0, respectively) to obtain 0.5 mM TMZ solutions. The solutions were stirred at 4 ℃ for 5 h, and were all stored as aliquots at 4 ℃, -20 ℃ and -80 ℃. By pipetting 150 μL samples into a 96-well plate in triplicate, the UV-Vis absorbance curves (200 to 400 nm) of three solutions were read by TECAN^{TM} Spark spectrometer at different time points: right after the preparation of 0.5 mM TMZ solutions (t_0), after 5 h stirring at 4 ℃ (5 h); and day 1, day 3 and day 5 after storage at three temperatures.

3.5 Encapsulation

3.5.1 Constructing EGFRa@AFt-TMZ system

Based on the study of Dr Bouzinab, the encapsulation was carried out on a molar ratio of 1:800 (protein cages:TMZ) [84]. Both human H-AFt and EGFRa@AFt samples were dialysed (20 mM tris, pH 3.5) overnight and the sample concentrations were adjusted with tris buffer to 2.0 mg/mL. TMZ DMSO solution (200 µL; 100 mM) was diluted in 1.8 mL tris buffer to obtain 10 mM stock. The TMZ stock was then added to protein sample (2.0 mg/mL) and the mixture was stirred for 5 h at 4 ℃. The volume relationship of 10 mM TMZ stock added to protein sample is shown as below:

$$\text{v (10 mM TMZ stock)} = \frac{1.6 \times 10^8}{\text{MW (protein sample)}} \times \text{v (protein sample) µL}$$

Theoretical concentrations of proteins and TMZ in encapsulated drugs would be:

	Protein concentration (µM)	**TMZ concentration (mM)**
EGFRa@AFt-TMZ	2.24	1.79
AFt-TMZ	2.69	2.15

Table 10: Concentrations of proteins and TMZ in encapsulated drugs.

The obtained drug solution was centrifuged at 4000 g, 4 ℃ for 4 min with spin filter (MWCO 30000 Da), then was diluted with tris buffer (20 mM, pH 3.5) to the original protein concentration measured and verified by NanoDrop™ Lite spectrophotometry. The drug solution was sterilised through 0.22 μm filter and aliquoted, stored at -20 ℃.

3.5.2 Encapsulation mimetic

Neutral red (NR) was prepared into a 10 mM stock and encapsulated by EGFRa@AFt as described in **3.5.1**. A sample of 1:800 molecule-protein molar ratio without 5 h encapsulation was also prepared as control. Native PAGE as described in 3.3 was adopted for fluorescence imaging. The two samples underwent electrophoresis in two separated gels at the same time to avoid excessive NR molecules diffusing among the gel matrix and causing disruption. After electrophoresis the gels were washed and imaged *via* UV-Vis transilluminator. The gels were then stained with Coomassie blue to indicate the protein bands location for comparison.

3.6 Mammalian Cell culture

3.6.1 Cells thawing

The growth medium was pre-warmed at 37 ℃ water-bath for 30 min before all cell culture processes. The cells were taken out from the cell bank and defrosted. Cell culture was carried in T25 cm^2 cell culture flasks with 6 mL growth medium. The defrosted cell suspension (1 mL) was added to the medium and gently swirled to distribute cells evenly. The cells were incubated at 37 ºC with 5% CO_2.

3.6.2 Cells passaging

Cells were ready to be passaged after reaching > 70% confluency. The consumed medium was aspirated, and the cells were washed gently with 3 mL of PBS. After PBS was aspirated, 0.5 mL of 1X trypsin (10X trypsin diluted with PBS buffer in 10% v/v, pre-warmed at 37 ℃) was added and spread out evenly to detach the cells. The flask was then incubated for 5 min (for U373 cell lines) or 10 min (for HCT-116 and MRC-5). Growth medium (4.5 mL) was added to deactivate the trypsin and suspend the cells. Cell suspensions (U373 cell lines, 500 µL; HCT-116 and MRC-5, 250 µL) were added to 6 mL medium in new culture flasks to start new passage, and again incubated at 37 ºC, 5% CO_2. The cells were experimented after 4 consistent passage generations and were stopped before 20 passages to maintain stable genetic characteristics.

3.6.3 Cells freezing

Cell lines were frozen down at an early passage (5 to 10). Cell lines at >70% confluency were washed with 3 mL PBS buffer and trypsinised by 1 mL trypsin and incubated for 5-10 min, then suspended in 1 mL of freezing medium (90% v/v FBS, 10% v/v DMSO). The cell suspension (1 mL) was introduced into a sterile cryogenic vial. The cells were frozen at -20 ℃ for 24 h, then transferred to - 80 ℃ for another 24 h, and finally stored in the liquid N_2 cell bank at -196 ℃.

3.7 Cell assays

3.7.1 Cell counting

The cell suspensions were prepared as described in **3.6.2** and were pushed through a needle-attached syringe 3 times to avoid cell clumping, then were vortexed for 30 s for an even distribution. Haemocytometer was used to determine cell density. Cell suspension (10 μL) was added to both sides of the haemocytometer then the cell numbers were counted manually under the microscope. As shown in Figure 14, in 3 randomly chosen 1 mm x 1 mm squares of both sides the cells were counted. The cell density of the suspension was determined by the equation below:

$$\text{cell density} = 10 \times \frac{\text{The sum of cell numbers of 6 squares}}{6} \text{ cells}/\mu\text{L}$$

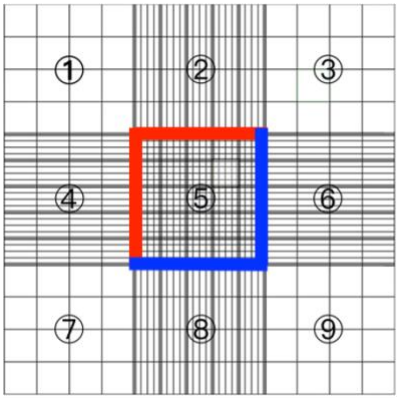


Figure 14. Layout of hemocytometer. All 9 areas marked are 1 mm x 1 mm squares. Within each chosen square, the cells lie on the red lines were counted while the ones on the blue lines were ignored.

3.7.2 MTT viability assay

The seeding suspensions were prepared by diluting the cell suspension with growth medium to desired density, and vortexed for 30 s for an even distribution (Table 11). The suspensions were seeded to 96-well plates with a multi-channel pipette. Wells on the plate edges were filled with 180 µL PBS to balance the medium evaporation rate. The plates were incubated at 37 ℃, 5% CO_2 overnight.

Cell lines	72 h exposure (cells/well, in 180 µL medium)	144 h exposure (cells/well, in 180 µL medium)
U373V/M	10000	10000
MRC-5	7500	2500
HCT-116	7500	2500

Table 11: Seeding densities of cell lines.

Cells were treated on the following day. Each testing agent were 10X serially diluted with blank medium for 4 times alongside blank medium as zero concentration control, then 20 μL of each concentration was added to cells in quintuplicate (Table 12). One plate was the T_0 control indicating the starting point of cell growth and cells were added with 20 μL blank medium then performed the MTT reaction. Other plates were incubated at 37 ℃, 5% CO_2 for 72 h or 144 h.

Testing agents	**Concentration (μM)**
EGFRa@AFt-TMZ	0.2~0.00002
AFt-TMZ	0.2~0.00002
EGFRa@AFt	0.2~0.00002
human H-AFt	0.2~0.00002
EGFR-affibody	4.8~0.00048
TMZ	500~0.05
DMSO (in v/v)	2%, 1%, 0.5%, 0.25%, 0.1%
20 mM, pH 3.5 tris (in v/v)	10%, 5%, 2.5%, 1%, 0.5 %

Table 12: Treatment concentration of each testing agent. All testing agents were filtered with 0.22 μm filter before treating the cells. The concentrations of both encapsulated drugs were determined based on the protein concentrations (see Table 10). The concentration of affibody was based on a 24-fold multiplication of protein concentration to mimic the extreme scenario that all affibodies on the cage surface encountering the receptors. All agents at top concentration were kept a ≤0.25% v/v DMSO and ≤5% v/v tris (20 mM, pH 3.5) concentration in the media of treated cells.

For MTT reaction, into total 200 μL medium of each well, 50 μL MTT reagent was added (2 mg/mL in PBS buffer; 0.4 mg/mL reacting concentration). The plate was incubated at 37 ℃, 5% CO_2 for 2.5 h to allow formazan formation. After incubation the solution in each well was aspirated and 150 μL of DMSO was added. The plate was orbitally shaken in the dark at 200 RPM for 10 min, then the optical density (OD) at 570 nm was recorded. For each cell line, the assay was repeated three times. The activities of the testing agents were represented by growth-inhibitory ability of 50% inhibition (GI_{50}), corrected by T_0 OD and calculated as followed:

$$\frac{\text{Control OD}_{570\text{ nm}} - \text{T}_0\ \text{OD}_{570\text{ nm}}}{2} + \text{T}_0\ \text{OD}_{570\text{ nm}} = \text{GI}_{50}\ \text{OD}_{570\text{ nm}}$$

The concentration at GI_{50} was estimated by interpolation. Data were analysed by one-way ANOVA and t-test functions of Graphpad Prism 9.0 software.

3.7.3 Clonogenic assay

The clonogenic assay was first trialed by seeding different numbers of both U373 cells on 6-well plates. The seeding numbers were 10000, 5000, 2500, 1000, 500 cells in 2 mL medium and the plate was incubated for 7 days to observe colony formation status. On day 3, the cells were washed with 1 mL PBS and medium in each well was refreshed. On day 7, cells were gently washed with 1 mL ice-cold

PBS buffer twice, then fixed with 1 mL methanol (99.8% v/v) for 10 min. After methanol was aspirated, 500 μL colony staining dye (0.05% v/v methylene blue in dH_2O) was distributed evenly to each well to stain the cells for 10 min. The excess stain was rinsed off by running water for 3 min. Each well was then observed under microscope to record the morphology of formed colonies, hence evaluating the proper seeding density for successful colonogenic assay.

3.8 Western blot

3.8.1 Collecting cell lysates

The lysis buffer [10X RIPA lysis buffer diluted with milli-Q water in 10% v/v (added with 1 tablet of protease inhibitor and phosphatase inhibitor); sterilised by 0.22 μL filter] and PBS buffer were cold on ice for 30 min. The cell suspensions were prepared as described in **3.6.3** and centrifuged at 4000 *g*, 4℃ for 10 min. After centrifugation the medium was aspirated, and the cell pellets were dispersed in 10 mL ice-cold PBS buffer and centrifuged again to wash off residual medium. The PBS wash was carried out twice. The cell pellets were then dispersed in 200 μL ice-cold lysis buffer and the mixture was left on ice for 30 min to allow the lysis to take place. The mixture was centrifuged at 3000 *g*, 4 ℃ for 10 min, then the obtained supernatants comprising the cell lysates were collected and stored at -80 ℃.

3.8.2 Bradford assay

The cell lysates were defrosted on ice for 2 h. BSA solution (10 mg/mL, 10 mg BSA in 1 mL milli-Q water) was serially diluted with milli-Q water by 10X to obtain a standard concentration ladder of 1, 0.8, 0.6, 0.4, 0.2, 0.1 mg/mL. The cell lysates were also diluted by 20X. Standard BSA ladder and diluted lysates (10 µL of each) were pipetted to a 96-well plate in triplicate and added with Bradford reagent (140 µL). The plate was shaken at 100 RPM in the dark for 10 min and OD at 595 nm was recorded. The standard BSA curve of OD against concentration was plotted, and the protein concentrations of the lysates were calculated based on the obtained curve. The volumes of lysates containing 50 µg protein were calculated and the sample volumes were topped up to 30 µL with lysis buffer.

3.8.3 Western blotting (Semi-dry transfer)

The preparation of SDS PAGE gel and electrophoresis procedure were same as described in section **3.3**. Lysates (30 µL) were mixed with 4X loading dye (10 µL) and heated at 90 ℃ for 5 min. The pre-stained protein ladder (10 µL) was loaded alongside 12 µL of samples into the wells and underwent electrophoresis. The resolving gel was carried onto the subsequent Western blotting.

Filter paper (8 pieces) and nitrocellulose membrane (1 piece) were trimmed to gel-size and soaked in 1X transfer buffer [10% v/v 10X transfer buffer (2.42% w/v tris, 11.3% w/v glycine in dH_2O), 20% v/v methanol (99.8%) in dH_2O] for 30 min. Western blotting was carried in Bio-Rad™ trans-blot turbo system. In transfer tank, from bottom to top the "transfer sandwich" was layered as: soaked filter papers (4 pieces), nitrocellulose membrane, the resolving gel, and the rest of filter papers (4 pieces). The transfer was carried out at 25 V, 2.5 A for 45 min.

3.8.4 Antibody incubation and imaging

The transferred membrane was blocked with 8 mL milk solution [2.5 g skimmed milk powder in 50 mL tris-buffered saline with Tween20 detergent solution (TBST solution; 0.8% w/v NaCl, 0.24% w/v tris, 0.1% v/v Tween 20 in dH_2O water)] and orbitally shaken at 100 RPM at room temperature for 1 h. The membrane was washed by soaking in TBST solution and shaken at 100 RPM for 5 min, then was incubated in primary antibody solution (8 µL EGFR recombinant rabbit monoclonal antibody, 8 mL milk solution; 1:1000 dilution) overnight at 4 °C, shaken at 100 RPM. On the following day, the membrane was washed for 3 times and incubated in secondary antibody (2 µL Goat anti-rabbit IgG secondary antibody in 8 mL milk solution; 1:4000 dilution) for 1 h at room temperature. The membrane was again washed and developed by evenly coating whole membrane with 1.5 mL ECL reagent in the dark for 5 min and then imaged.

4. Results & discussion

4.1 Protein expression

4.1.1 Protein extraction

The *E. coli* protein-expression system serves as an excellent laboratory protein production method for its rapid growth and low cost. The TUNER™ *E. coli* strain was designed to optimise protein-folding ability by controlling IPTG entrance into the cell, which limits the protein-expression rate to increase the amount of correctly folded AFts [89]. The affibodies due to their short sequence were more easy-folding and soluble. After breaking down the bacterial membrane by sonication, they were subsequently collected in the soluble fraction, while the overexpressed large AFts nanocages were however still misfolded and aggregated into inclusion bodies which were pelleted.

Dissolving the pellets with buffer of high-concentration urea helps to solubilise the mis-folded protein. The SDS PAGE gel shows the difference between sonication and urea extraction of EGFRa@AFt (Figure 15). In practice, each electrophoresis samples were 4X diluted with elution buffer A, for large amounts of proteins in samples would result in stacking in the gel matrix. As anticipated, the soluble fraction from sonication contained no protein of interest at the correct MW (EGFRa@AFt subunits MW 30.5 kDa), while the insoluble buffer successfully solubilised the protein into the urea soluble fraction with an evident

band. Through this method, the excessive cations from the cell pellets were also released into the protein extractions, which would affect affinity-binding during purification. The cations were removed by chelation with 0.05 M EDTA during dialysis and the protein structure was also naturally restored in the suitable buffer (20 mM tris, pH 9.0). It was noticed that a minor loss still occurred after urea extraction, nevertheless, both AFts were successfully expressed and primarily extracted in satisfying yields and were carried onto the following procedures.

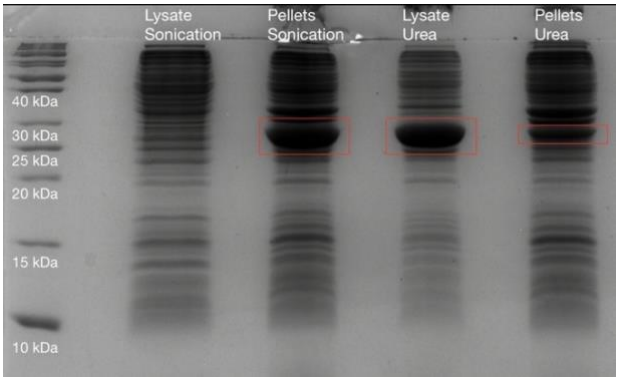


Figure 15: SDS PAGE gel image for extraction of EGFRa@AFt.

4.1.2 Purification results

His-tags® exhibit strong chelating affinity towards transition metal cations such as Cu^{2+} and Ni^{2+}. Hence the His-tags®-modified subunits of AFts would bind with immobilised Ni^{2+} stronger than other impurities in the lysis and would only be replaced from the column with high concentration of imidazole which competes this affinity [90]. For Ni^{2+} affinity purification, as shown in Figure 16, both AFts were successfully collected at 70% buffer B fractions and most impurities were separated into the flow-through (Figure 16: A, B). The high protein concentration

in the 70% sample disrupted the nearby bands, especially the 100% fraction, which was also collected based on the observation of sample trace in the 100% fraction in a pilot trial (Figure 16: F). AFts in fractions under 70% were discarded as they were contaminated by binding with other impurities, hence they were displaced at low imidazole concentrations due to weakened column-binding affinity. The affibody was collected at 8% and 10% fractions. 5% was discarded due to the noticeable background impurities (Figure 16: E). Collected samples were dialysed to remove imidazole.

Both AFts samples were then purified as subunits of negative charges (dissembled at pH 12) *via* anion-exchange chromatography in case the protein cages containing the *E. coli* membrane component lipopolysaccharide (LPS) from the cell wall lysis, which is an endotoxin that causes oxidative damage to the cells hence potentially affects the assay experiments [91]. According to Isobel Holden, the LPS could be displaced with > 600 mM NaCl while the relatively weakly-bound AFts were mostly eluted with lower NaCl concentration (10%~50% fractions and flow-through) (Figure 16: C, D) [92].

From 1 L *E. coli* culture, the final yields for both AFt were ~40 mg. Yet during the Ni^{2+} affinity purification, the losses of proteins of interests in the flow-through fraction were observed (Figure 16: A, B). This was due to the limited binding capacity of Hitrap™ chelating HP column (~12 mg/mL resin, ~60 mg protein-

binding capacity for 5 mL column) [93], thus after the column was saturated, the overloaded proteins were wasted in the flow-through fraction. This could be optimised by stacking two Hitrap^{TM} columns to increasing the binding surface to minimise the loss.

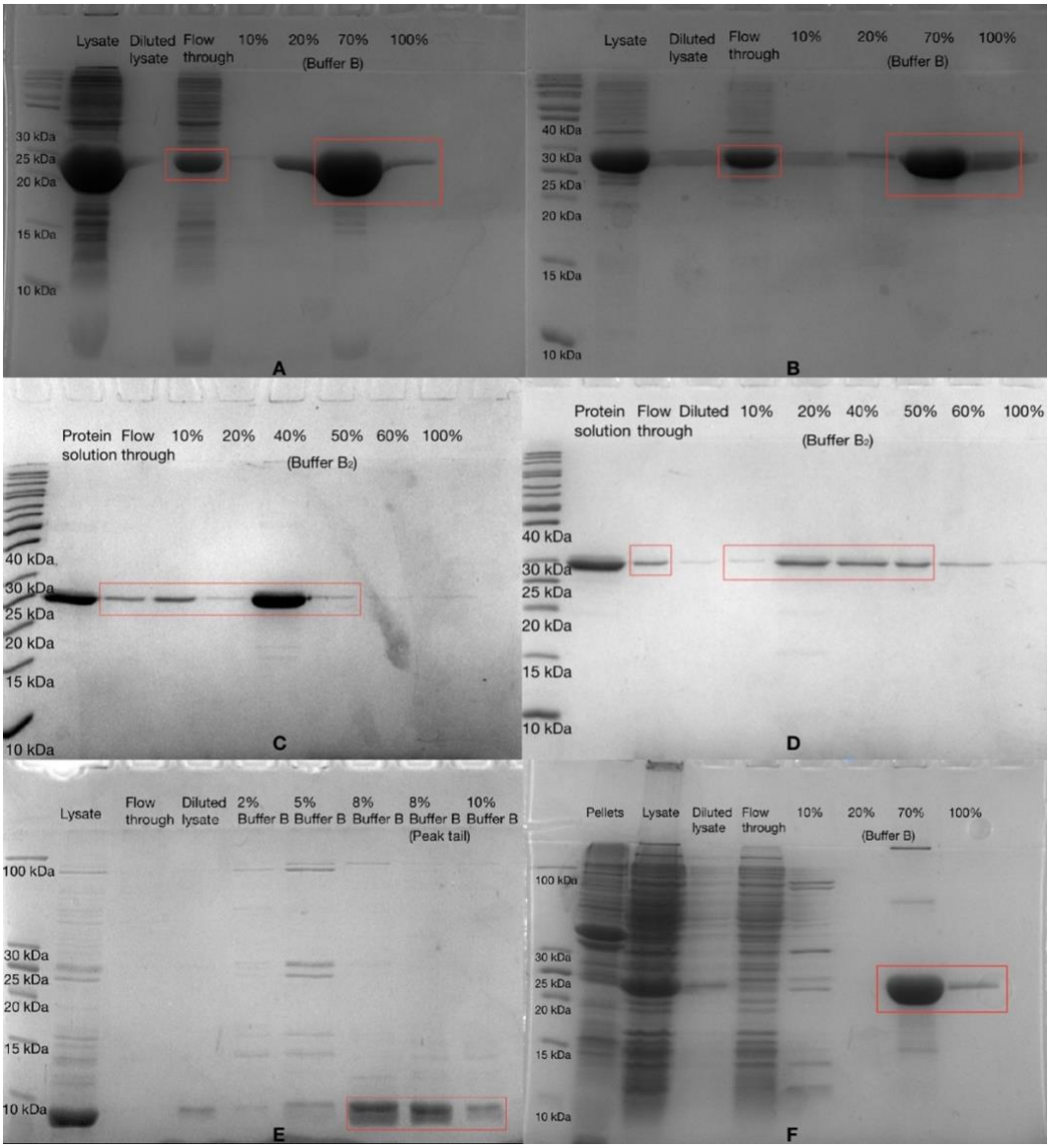


Figure 16: SDS PAGE gel images for lysate extraction and protein purification. Nickel affinity purification of (A) human H-AFt (human H-AFt subunit MW 24.3 kDa), (B) EGFRa@AFt, (E) EGFR-affibody (8.5 kDa), (F) Human H-AFt purification pilot trial; Anion-exhange purification of (C) human H-AFt, (D) EGFRa@AFt. Protein collected are marked in the red box.

4.2 Verification of encapsulation

4.2.1 TMZ stability curves

Based on the calculations carried out by Protein Calculator programme (v3.4) [94], the pI values for both human H-AFt and EGFRa@AFt are 5.9 and 5.52, respectively. Both AFts (2 mg/mL) were found soluble in 20 mM pH 3.5 tris buffer (also at pH 6.5 for EGFRa@AFt). Hence, it was necessary to investigate the long-term stability of TMZ under different pH conditions to find out ideal encapsulation and storage conditions.

As shown in Figure 17, in pH 3.5 tris buffer (20 mM), TMZ retained its stability for 5 days under all storage temperatures. Furthermore, in a pH 6.5 buffer (where the pH value is near the neutral pH 7.0), at 4 ℃, TMZ gradually degraded at a slow rate that only around 13% ($P < 0.05$) was hydrolysed on day 5. It has also been demonstrated that at -20 ℃ and -80 ℃ storage conditions the degradation stopped. In contrast, when TMZ was in a basic environment (pH 8.0), a distinct degradation was observed at 4 ℃ which was reflected by the appearance of AIC absorbance maxima peak at 265 nm and the decline of both TMZ peaks at 330 nm and 257 nm (Figure 17: D, E, F). After 5 h only around ~ 45% ($P < 0.0001$) of TMZ remained and a full degradation was observed after 5 days when stored at 4 ℃. Additionally, it was noticed that -80 ℃ helped halt the degradation process at pH 8.0 that ~ 42% of TMZ remained after 5 days ($P < 0.0001$). Therefore,

under acidic conditions, the long-term stability of TMZ was proved. The encapsulation for both AFts was proposed to take place at pH 3.5 for consistency in environment pH and all three storage temperatures (4 ℃, -20 ℃, -80 ℃) were found suitable to store the encapsulated drugs.

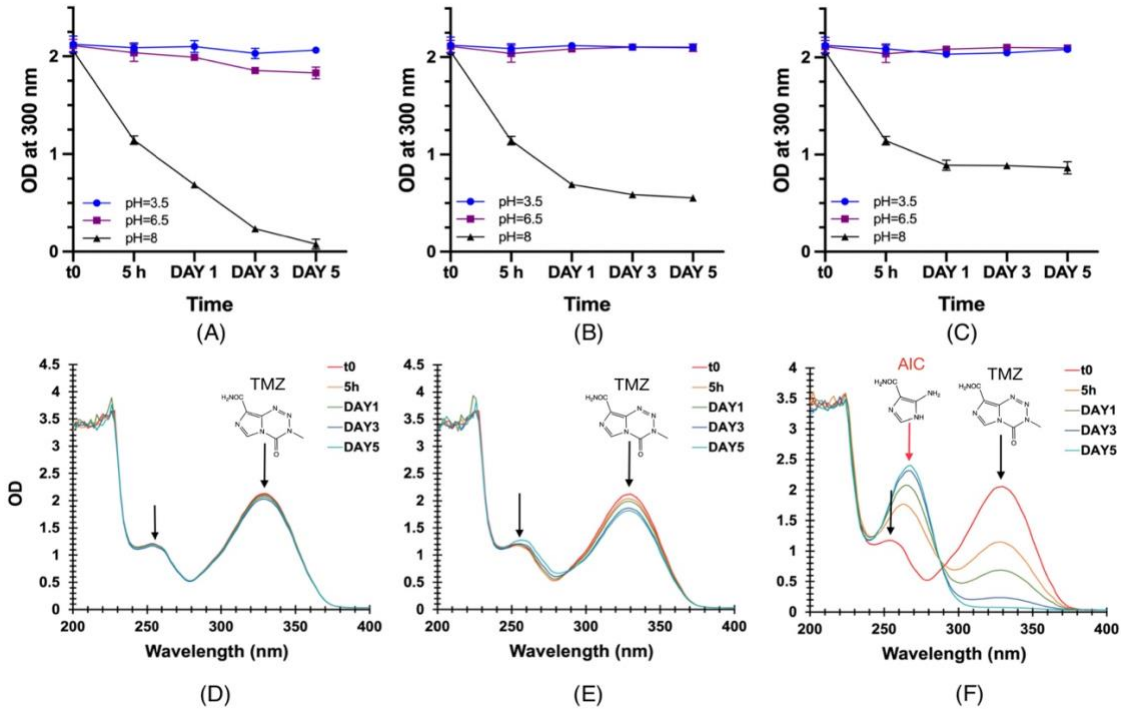


Figure 17: OD330 plots and stability curves (200~400 nm) of 0.5 µM TMZ under different pH values and storage conditions in 20 nM tris buffer. The three OD330 plot graphs are TMZ of three pH values under different storage conditions: (A) 4 ℃, (B) -20 ℃, (C) -80 ℃, data are reported as mean ± SD (measurements were performed in triplicates); Stability curves are TMZ at 4 ℃: (D) pH 3.5, (E) pH 6.5, (F) pH 8.0.

4.2.2 Structure integrity of EGFRa@AFt and human H-AFt

The native PAGE allows analysed AFts to maintain their quaternary cage structures, thus it is an ideal method to evaluate the structural integrity of proteins under different conditions. Based on the findings of Isobel Holden, in 20 mM tris buffer the disassembly of both human H-AFt and EGFRa@AFt were only witnessed at pH 3.0 and lower [92]. The samples of both AFts were dialysed overnight in tris buffers of different pH values (20 mM, pH 3.5/9.0). As shown in Figure 18, comparing to the 20 mM pH 9.0 tris buffer where the compact proteins structures were naturally maintained, no disassembly was observed for both human H-AFt and EGFRa@AFt at pH 3.5. This method could be further optimised by using commercial horse spleen/human AFt as a standard reference to the recombinant huamn H-AFt samples if avaiable. It should be noticed that pH 3.5 tris buffer was mainly adopted as a consistent buffer variable even though it was out of tris buffer working pH range (pH 7.0-9.0).

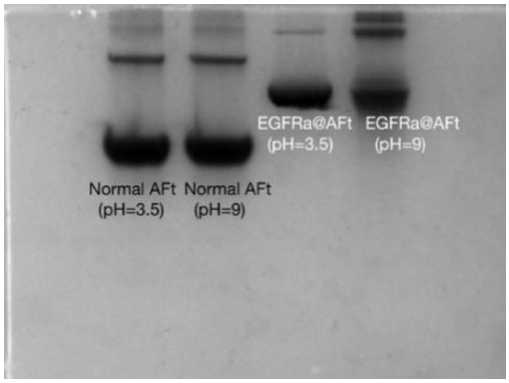


Figure 18: Native PAGE gel images for EGFRa@AFt and human H-AFt stored in 20 mM tris buffer with different pH values (pH 3.5/9.0).

4.2.3 Encapsulation mimetic

According to Dr Bouzinab, 5 h of diffusion-encapsulation manages to encapsulate ~500 TMZ molecules per AFt cage [85]. However, a visualization method to definitively show encapsulation of TMZ within the nanocage was elusive due to the rapid diffusion of drug molecules in an aqueous environment. Also, TMZ can only be detected as free molecules *via* methods such as mass spectroscopy that is not applicable to systems as complex as encapsulation inside protein nanocages. An alternative molecule of similar size and structure with TMZ – neutral red was suggested to present and verify the encapsulation mechanism as it can be observed under UV-Vis *via* its fluorescence characteristic (Figure 19).

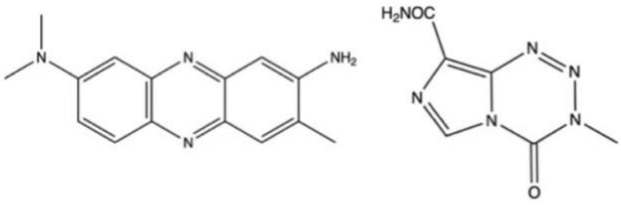


Figure 19: Structural comparison between NR and TMZ molecules. Although NR processes one more ring structure to TMZ, the size is still negligible in comparison to the 3-4 Å protein ion channels.

EGFRa@AFt was chosen for this experiment. It was hypothesised that if there was no interaction allowing NR to bind with protein subunits, NR in the control group (no encapsulation; NR molecules remained outside the nanocages in the background buffer) would be expelled out of the gel matrix by electric currents

during electrophoresis, hence under UV-Vis no fluorescence would be observed at the band which indicating protein nanocages on the native PAGE gel; and if NR molecules diffused into the nanocages *via* 5 h encapsulation, after electrophoresis the protein band of the encapsulation mixture would exhibit fluorescence from the NR molecules caged inside.

The results showed that the encapsulation mixture successfully exhibited a faint fluorescent band (NR molecules inside EGFRa@AFt) which was validated by the stained gel (Figure 20: A, B). For the control group which underwent no encapsulation, only traces of NR molecules irregularly diffusing among the gel matrix (gel was unevenly fluorescent) and a faint fluorescent electrophoresis trail were observed (Figure 20: C, D). As the NR and protein in the control group were only combined moments prior to electrophoresis, this demonstrated that no formation of fluorescent band would be observed when NR were analysed as free molecules *via* electrophoresis.

However, this indirect method only provides evidence that unspecified NR-protein interaction was induced during the encapsulation process, which could not be deducted that the NR molecules were encapsulated within the protein cages, for it remains unclear if any non-specific forces existed between the two molecules such as circumstance where NR molecules were adherent to the cage outer surface. To improve this method, an additional control group should be considered: as

EGFRa@AFt would disassemble at pH < 3.0, by mixing the EGFRa@AFt subunits with NR molecules for 5 h and analysing the consequent mixture *via* Native PAGE, the potential non-specific interaction between the protein and NR molecules could be verified according to the florescence status of the corresponding band which indicates the subunits.

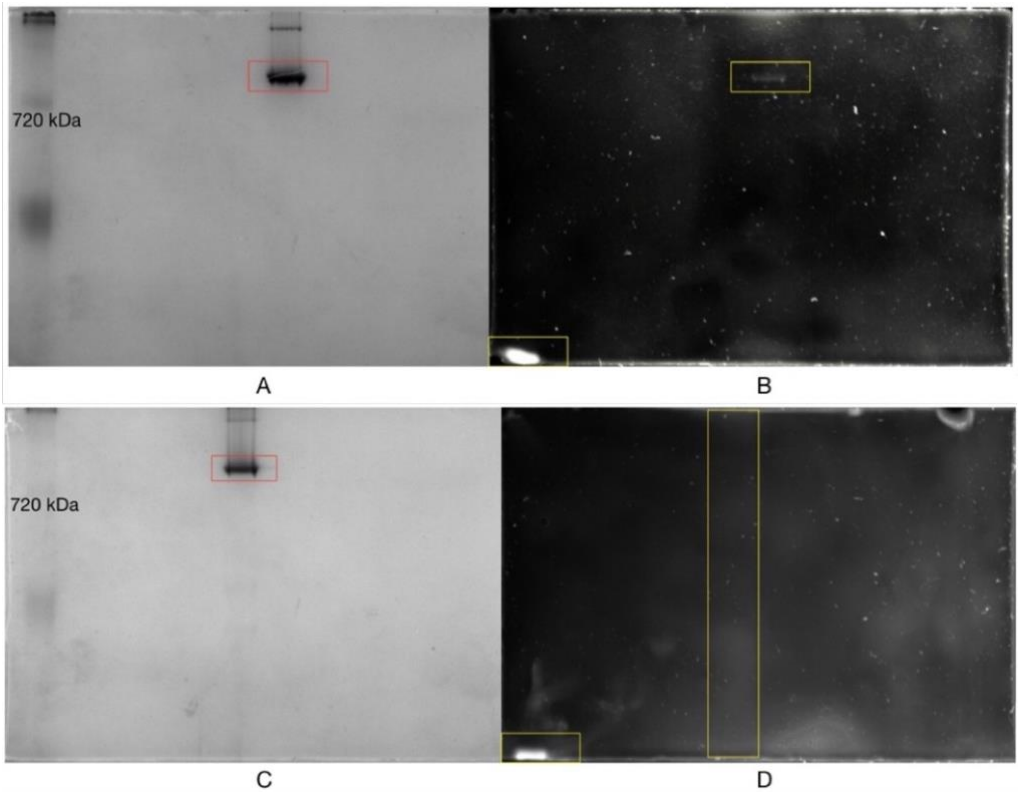


Figure 20: Native PAGE images under white light and UV-Vis. (A), (B): NR encapsulation system mimetic; (C), (D): Control group without encapsulation (MW of EGFRa@AFt was 732 kDa).

4.3 EGFR expression

In previous study of Dr Bouzinab, *via* western-blot, both U373 cell lines and HCT-116 were detected with overexpressed TfR1 (while untraceable for MRC-5)

and only U373M was found with high-level MGMT [85]. Here, the same method was also purposed to evaluate the EGFR expression status of the chosen cell lines.

During Bradford assay, it was noticed that from the cell cultures grown in T25 cm^2 flasks, the extracted lysates contained rather lower protein concentrations than the required amount described in section **3.8.2**. All lysates were hence prepared into 30 μL samples containing 20 μg proteins. This could be optimised by preparing cell lysates from a larger culture grown in T75 cm^2 flask. The best fit of Bradford assay standard curve is shown as Figure 21, and the protein concentrations of cell lysates are shown in Table 13.

As shown in Figure 22, the EGFR abundancy was quantified based on the relative signaling intensity *via* Image Studio™. EGFR was expressed on both U373 cell lines with U373V showed higher expression level over U373M. HCT-116 cell line presented highest expression level, while was untraceable for MRC-5 cell line which might only contain low EGFR concentration from its regulated *EGFR* oncogene expression. During the time of experiment, only the EGFR primary antibody was available. Although the EGFR expression status of four cell lines was determined, to rule out the man-errors in sample preparation, the primary antibody of glyceraldehyde 3-phosphate dehydrogenase (GAPDH) should be introduced. GAPDH is universally expressed in all cell types, thus can be seen as a “house-keeping” marker to quantify the loaded samples [95]. Moreover, the pre-

stained protein ladder was also transferred onto the membrane, which could be highlighted by chemiluminescent marker to indicate the MW of the obtained protein bands if available. Therefore, a precise comparison of EGFR expression status of four cell lines could not be suggested.

Cell lines	Protein lysates (mg/mL)
U373V	1.98
U373M	1.42
MRC-5	0.713
HCT-116	1.86

Table 13. Protein concentrations of cell lysates.

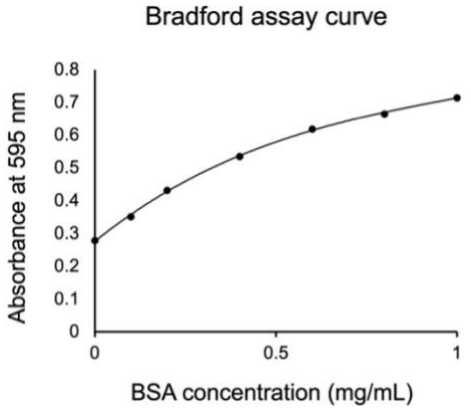


Figure 21: BSA standard curve. The curve equation was found to be $y=0.213x^3-0.656x^2+0.880x+0.277$ ($R^2=0.999$).

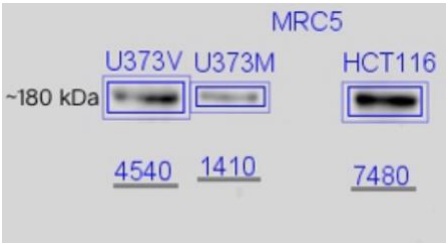


Figure 22: Western blot image of EGFR expression on U373, MRC-5, and HCT-116 cell lines. The numbers below the blue boxes are the relative quantification of EGFR of corresponding cell lines.

4.4 Cell assays

4.4.1 *In vitro* activity (MTT assay)

Various studies have already discovered the potential targeting methods for TMZ delivery against TfR1 *via* different molecule vehicles, such as TfR1 antibody fragments-functionalised liposome and horse spleen AFt. Aside from their promising abilities for drug-loading and cancer-targeting, they have also presented enhanced *in vitro* activities towards GB cells over free TMZ molecules by ~2-3 orders of magnitudes [85] [96]. Although due to the difference in experimental methods, a direct comparison between the MTT assay results of these studies and the current experiment could not be suggested, still, they provide a reference in evaluating the level of enhanced activity of EGFRa@AFt-TMZ.

The growth inhibition activities of EGFRa@AFt-TMZ, AFt-TMZ, free TMZ, and other vehicle agents [EGFRa@AFt, EGFR-affibody, human H-AFt, DMSO and tris buffer (20 mM, pH 3.5)] were investigated by 72 h MTT assays *via* four cell lines (U373V/M, HCT-116 and MRC-5). Due to the limitation of experiment time, the 144 h assays were solely tested with EGFRa@AFt-TMZ, EGFRa@AFt and TMZ on U373V/M and MRC-5. The GI_{50} of all agents for two assays of different incubation time were obtained and summarised in Table 14.

Cell lines	GI_{50} (72 h)		
	EGFRa@AFt-TMZ	AFt-TMZ	TMZ
U373V	8.18 ± 1.67 pM	5.77 ± 1.52 nM	63.2 ± 18.3 µM
U373M	44.56 ± 1.97 pM	1.56 ± 0.97 nM	314.2 ± 92.28 µM
HCT-116	1.47 ± 0.10 nM	21.54 ± 7.79 nM	> 500 µM
MRC-5	0.10 ± 0.032 µM	0.21 ± 0.01 µM	280.95 ± 44.84 µM

Cell lines	GI_{50} (72 h)			
	EGFRa@AFt	human H-AFt	EGFR-affibody	DMSO
U373V	4.46 ± 1.11 nM	76.72 ± 61.08 nM	4.40 ± 2.48 µM	>0.25%
U373M	3.97 ± 2.25 nM	81.19 ± 64.29 nM	> 4.8 µM	>1%
HCT-116	> 0.2 µM	> 0.2 µM	> 4.8 µM	>1%
MRC-5	> 0.2 µM	> 0.2 µM	> 4.8 µM	>0.5%

Cell lines	GI_{50} (144 h)			
	EGFRa@AFt-TMZ	TMZ	EGFRa@AFt	DMSO
U373V	0.37 ± 0.26 nM	96.65 ± 6.72 µM	29.48 ± 16.08 nM	>0.5%
U373M	0.12 ± 0.040 nM	> 500 µM	30.42 ± 21.35 nM	>1%
MRC-5	170 ± 37.62 nM	> 500 µM	> 0.2 µM	>1%

Table 14: GI_{50} values of all testing agents for 72 h assays; GI_{50} of EGFRa@AFt-TMZ, TMZ, EGFRa@AFt and DMSO for 144 h assays. Data are reported as mean ± SD [each agent were tested in quintuplicate in one trail (n=5), 3 trials were repeated].

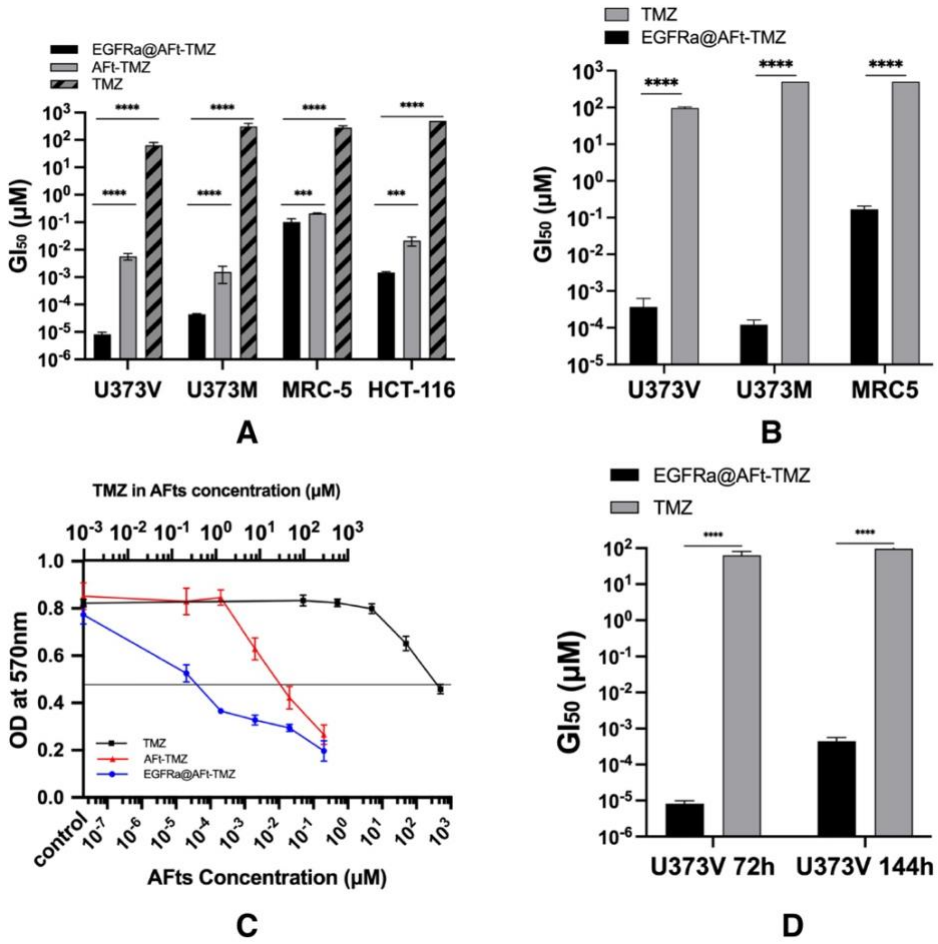


Figure 23: GI_{50} of EGFRa@AFt-TMZ, AFt-TMZ, and TMZ for (A) 72 h assay, (B) 144 h assay; (C) Growth-inhibition profile against U373V 72 h assay; (D) GI_{50} comparison of EGFRa@AFt-TMZ and TMZ for U373V 72 h and 144 h assays. In (A) and (B), the GI_{50} values of TMZ > 500 μM were represented as 500 μM for comparison. Plot data was reported as mean ± SD (n=5, 3 trials were repeated). Values of *P < 0.05, **P < 0.01, ***P < 0.001, and ****P < 0.0001 were considered as statistically significant compared to the TMZ group. See **Appendix** for all Growth-inhibition profiles.

Based on the 72 h assays, EGFRa@AFt-TMZ exhibited significantly enhanced growth-inhibitory ability compared to AFT-TMZ and free TMZ molecules (Figure 23: A, B; P < 0.001 and P < 0.0001). It was also discovered that EGFRa@AFt-TMZ showed a significant effectiveness at pM concentrations in both U373 cell

lines after 72 h and 144 h incubations (though longer incubation time increased the GI_{50} values by ~2 orders of magnitude; $P < 0.0001$), while barely exerting any growth-inhibitory effects towards MRC-5 cells at concentrations < 20 nM (Figure 23: D; growth inhibition profiles in **Appendix**). These findings suggested that EGFRa@AFt-TMZ system has promising potentials of *in vitro* targeting towards EGFR-overexpressed GB cells and an enhanced drug activity, also overcoming the MGMT-driven resistance to TMZ. Even though EGFRa@AFt-TMZ also succeeded in showing significantly improved growth-inhibitory ability over free TMZ molecules in HCT-116 cell line (Table 14; Figure 23: A, $P < 0.0001$), however, HCT-116 showed minor difference in responses towards two delivery systems. This suggested that even an enhanced drug activity might be achieved by the delivery system, the cells with inactive MRR mechanism might possess better tolerance towards DNA methylation.

It was also observed that EGFR-affibody and EGFRa@AFt exhibited growth-inhibitory effects towards U373 and HCT-116 EGFR-overexpressed cell lines (Table 14; **Appendix)**. The large amount of EGFR-affibody at high concentrations (~4.8 μM) might compete with the growth factors in ligand-binding with the receptors, hence hindered the downstream signaling pathways which promote the cell proliferation and cell growth. For EGFRa@AFt (> 20 nM), as mentioned in **1.3.2** and **1.4.2**, the EGFR trafficking mechanism served an essential role in regulating the signaling pathways, which involved the

endocytosis of receptors [97]. Due to the multiple affibodies on the protein surface, upon recognition, it was assumed that an EGFRa@AFt molecule could bind with multiple receptors and undergo endocytosis to enter the early endosome together. The "endosome escape" nature of the protein might inhibit the recycling process of the receptors, which eventually lower the receptor density on cell surface and limit the cell proliferation and growth. The growth inhibition effect of Human H-AFt towards both U373 cell lines at high concentration (> 50 nM; Table 14, **Appendix**) was noticed. It was also reported that the overexpression of TfR1 was frequently observed in GB cells including U373 cell lines [85] [98]. A study discussed a potential cause that the H subunits of recombinant human H-AFt might bind with free iron ions "pool". During endocytosis of TfR1 bound to AFt, the human H-AFt which enters the acidic environments in mature or late endosomes would release the bound iron ions as Fe^{2+}, hence causing oxidative damage to the cells [99]. These theories on endocytosis also suggested that the effectiveness of the delivery systems might also benefit from the acidic environments (pH 5.6-6.0) during endocytosis to stabilise TMZ molecules.

To conclude, the EGFRa@AFt-TMZ system showed significant *in vitro* growth-inhibitory ability and enhanced drug activity at low concentration levels towards U373 cell lines over AFt-TMZ system and free TMZ molecules ($P < 0.0001$), and barely affected normal cells at these concentration levels. These data suggested EGFRa@AFt an enhanced *in vitro* drug activity and targeting ability against

EGFR-overexpressed GB and the potentials to overcome MGMT-mediated TMZ resistance. Further investigations are required to determine possible limitations imposed by MMR-deficiency on the growth-inhibitory performance of the TMZ.

4.4.2 Colony formation of U373 cells

Upon its development in 1956, clonogenic assay has been widely adopted to examine the reproduction ability of treated cancer cells as a single cell could form a visible "colony" with its surrounding progenies [100]. The number of successfully formed colonies hence reflects the growth inhibition ability of the treatments. Therefore, it serves as a parallel method to corroborate the findings of MTT assay experiments at a larger scale. Generally speaking, a cell colony comprises ≥ 50 cells generated from a single cell. Thus, to form dispersed colonies on 6-well plate, a low seeding density is required (usually ≤ 1000 cells/well) [101].

Based on the previous study of Dr Bouzinab, successful clonogenic assays for U373 cells were conducted with a seeding density of 600 cell/well and were incubated for 6 days while exposed to different treatments (human H-AFt, AFt-TMZ and free TMZ molecules) [85]. However, during cell passaging described in **3.6.2**, the current U373 cell lines were observed a relatively slow proliferation rate that 70% confluency was only reached after ~8 days incubation, while HCT-116

and MRC-5 cell lines became 70% confluent in < 5 days. Moreover, their unique elongated spindle shapes remained a doubt whether this morphological characteristic would eventually allow colonies to be formed (Figure 24: A). Hence, due to the lack of experiment time, a short-term pilot trial was performed to evaluate the viability of colony formation.

After 1 week incubation of U373V, in the wells of high seeding densities (10000 and 5000 cells), the cells easily grew to "meet" the adjacent cells as graph A in Figure 24, where no distinguishable colonies were observed. At lower densities (2500 and 1000), as shown in the red squares of graph B and C, a few colonies were formed but only with ~40 cells and the majority of cells grew into irregularly scattered small clusters and showed a tendency of "reaching out" to the nearby cells. When seeded with lowest density (500 cells), the proliferation rate of cells evidently slowed down. It was assumed that U373 cell lines demand higher seeding number to accelerate the proliferation process as *in vitro* cells were found requiring certain level of density for adequate intercellular signaling and receptor trafficking [102]. Therefore, the original seeding method purposed by Dr Bouzinab was not applicable for this research, for that the number of post-treatment cells would be lower than 500 and would not effectively form colonies in 6 days. A higher seeding number (~1000) and longer incubation time (~ 2 weeks) should be considered for both U373 cell lines to further investigate the methods for successful clonogenic assays.

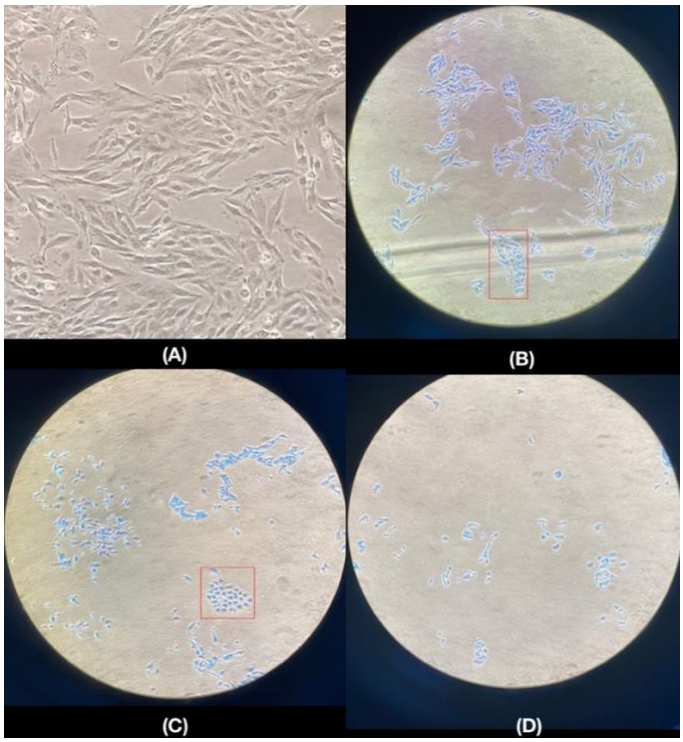


Figure 24: Images for U373V cell line. (A) Picture of U373V cells in cell culture flask; The stained cells of clonogenic assay with different seeding density: (B) 2500, (C) 1000, (D) 500. Distinguishable colonies (<50 cells) are marked with red squares. Two U373 cell lines share identical morphological characteristics.

5. Conclusions & Future works

In this study, the recombinant EGFRa@AFt, human H-AFt, and EGFR-affibody were successfully expressed and purified from *E. coli*; The structural integrities of both AFts and long-term stability of TMZ under encapsulation condition (20 mM, pH 3.5 tris buffer; 4°C) were demonstrated. The strong chemical tolerance of both recombinant AFts presented possibilities for various study to be carried out under different conditions; TMZ molecules were successfully encapsulated with both AFts through diffusion *via* the protein surface channels by mixing the two components at 4°C for 5 h. The potential of purposed encapsulation-memetic system allowed a further investigation on qualifying this diffusion-encapsulation scheme; Based on Western blot, the expression of EGFR on three cancer cell lines (U373V/M and HCT-116) was proved, while MRC-5 possesses untraceable EGFR level; After 72 h or 144 h incubation of *in vitro* MTT assays, for EGFR-overexpressed U373V cell line, tested by GI_{50} values, the EGFRa@AFt-TMZ system exhibited significant growth-inhibitory ability (8.18 ± 1.67 pM, 72 h; 0.37 ± 0.26 nM, 144 h) over AFt-TMZ system (5.77 ± 1.52 nM, 72 h) and free TMZ molecules (63.2 ± 18.3 μM, 72 h; 96.65 ± 6.72 μM, 144 h) ($P < 0.0001$), indicating an enhanced TMZ activity; The isogenic U373M cell line showed similar responses, suggesting that EGFRa@AFt-TMZ delivery system possess a potential to overcome TMZ resistance conferred by MGMT. EGFRa@AFt-TMZ has little effect on the growth of non-tumourigenic MRC-5 < 20 nM, providing evidence that EGFRa@AFt-TMZ offers enhanced *in vitro* targeting ability. The

response of HCT-116 cell line to EGFRa@AFt-TMZ also found a significantly enhanced growth-inhibitory effect over free TMZ (72 h; 1.47 ± 0.10 nM and > 500 μM, respectively; $P < 0.0001$). However, it showed only slight improvement compared to AFt-TMZ system (21.54 ± 7.79 nM, 72 h), suggesting that despite an enhanced drug activity was achieved, the TMZ mechanism of action might be largely limited by MRR activities of the cells. These findings suggested a promising foreground for EGFRa@AFt to be adopted in clinical application to provide a more efficient and less harmful treatment method for EGFR-overexpressed diseases. This potential for multi-functionalisation and targeting ability of recombinant AFt shows infinite possibilities in the ground of nanotherapeutics, not only for drug-delivery, but also cell imaging and so on.

For future directions, there are more investigations should be considered to investigate the working mechanism and limitation of EGFRa@AFt-TMZ and to explore more possibilities in utilising EGFRa@AFt as a GB-targeted molecule cargo:

- **Investigating MMR-level limitation**

  Studies have shown that MMR-deficient cancer cells tend to exhibit resistance more rapidly towards chemotherapy treatment [103], which agrees with the findings of this research. To further prove the importance of MMR mechanism activity in evaluating the performance of TMZ, an isogenic HCT-116 cell line

with high MMR level can be adopted to compare the responses to both drug-delivery systems with current results.

- **Detecting DNA methylation and breakdown in treated cells**

  To validate the DNA methylation induced by EGFRa@AFt-TMZ system, the indirect enzyme-linked immunosorbent assay (indirect ELISA) should be adopted to specifically detect and quantify the *O*6-MeG adducts level of methylated DNA strands [85]. The γ-H2AX foci assay can also be utlised to investigate the DNA damage status of the treated cells, which allows the detection of the breakdown of DNA double-strands to reflect the activity of MMR mechanism [104]. By comparing with cells treated with AFt-TMZ system and free TMZ molecules at same concentration level, these methods will help corroborate whether the enhanced drug activity and MGMT-overcome were achieved by elevated intracellular TMZ-accumulation delivered *via* EGFRa@AFt-TMZ system.

- **Verifying cell death mechanism**

  It has been reported that instead of programmed apoptosis, TMZ in fact induces autophagy-dependent cell death (autophagic apoptosis) in GB treatment, both *in vivo* and *in vitro* [105]. Although detailed mechanism of autophagic apoptosis is not yet clear, it is possible to verify its induction by introducing inhibitor of light chain 3 (LC 3). LC 3 is a microtubule-associated protein, whose expression-elevation and aggregation are always found during autophagic activities. Its

inhibition was reported to elevate the *in vitro* GB cell viability after exposure to TMZ, which helps indirectly indicate the autophagic apoptosis induced in treated cells [106].

Also, apoptosis assay should be considered to validate that no necrosis was contributed from the EGFRa@AFt-TMZ system. Propidium iodide is allowed to penetrate cell membrane and bind to the DNA in both necrotic and apoptotic cells; while phosphatidylserine as an inner cell membrane lipid is only exposed to the outer membrane upon apoptosis (both programmed and autophagic), which hence allows its specific binding with protein Annexin V to occur. Together, the combined fluorescence signals from these specific bindings can be detected and quantified by flow cytometry method, thus the overall cell death status can be visualised [107].

- **Encapsulating TMZ analogues**

  After years of development, many TMZ analogues are now available with different chemical characteristics, such as a derivative with N^3-methyl substituted by propargyl (N3P). This TMZ derivative possesses greater potency and is capable of overcoming resistance to TMZ mediated by MGMT and actively inducing autophagic apoptosis in malignancies which resist programmed apoptosis. However, N3P suffers from a shorter plasma half-life (49 min). It has been proved that by encapsulating N3P with horse spleen AFt, the *in vitro* growth-inhibitory ability of the encapsulated system against U373 cell lines was

significantly improved ($P < 0.0001$) [85][108]. If offers a promising prospect that encapsulating N3P into EGFRa@AFt may further enhance the growth-inhibition on GB cell lines even superior to current EGFRa@AFt-TMZ system.

6. Reference

1. Ostrom, Q. T.; Gittleman, H.; Farah, P.; Ondracek, A.; Chen, Y.; Wolinsky, Y.; Stroup, N. E.; Kruchko, C.; Barnholtz-Sloan, J. S. CBTRUS Statistical Report: Primary Brain and Central Nervous System Tumors Diagnosed in the United States in 2006-2010. *Neuro Oncol* **2013**, *15 (Suppl 2)*, 1–56. doi:10.1093/neuonc/not151.

2. Witthayanuwat, S.; Pesee, M.; Supaadirek, C.; Supakalin, N.; Thamronganantasakul, K.; Krusun, S. Survival Analysis of Glioblastoma Multiforme. *Asian Pac. J. Cancer Prev.* **2018**, *19*, 2613–2617. doi:10.22034/APJCP.2018.19.9.2613.

3. Poon, M. T. C.; Sudlow, C. L. M.; Figueroa, J. D.; Brennan, P. M. Longer-Term (≥ 2 Years) Survival in Patients with Glioblastoma in Population-Based Studies Pre- and Post-2005: A Systematic Review and Meta-Analysis. *Sci Rep* **2020**, *10*, 11622. doi:10.1038/s41598-020-68011-4.

4. Thakkar, J.P., Dolecek, T.A., Horbinski, C., Ostrom, Q.T., Lightner, D.D., Barnholtz-Sloan, J.S. and Villano, J.L. (2014). Epidemiologic and Molecular Prognostic Review of Glioblastoma. *Cancer Epidemiol. Biomark. Prev* **2014**, *23*, 1985–1996. doi:10.1158/1055-9965.epi-14-0275.

5. Tian, M.; Ma, W.; Chen, Y.; Yu, Y.; Zhu, D.; Shi, J.; Zhang, Y. Impact of Gender on the Survival of Patients with Glioblastoma. *Biosci Rep* **2018**, *38*, BSR20180752. doi:10.1042/BSR20180752.

6. Patel, A. P.; Fisher, J. L.; Nichols, E.; Abd-Allah, F.; Abdela, J.; Abdelalim, A.; Abraha, H. N.; Agius, D.; Alahdab, F.; Alam, T.; Allen, C. A.; Anber, N. H.; Awasthi, A.; Badali, H.; Belachew, A. B.; Bijani, A.; Bjørge, T.; Carvalho, F.; Catalá-López, F.; Choi, J.-Y. J. Global, Regional, and National Burden of Brain and Other CNS Cancer, 1990–2016: A Systematic Analysis for the

Global Burden of Disease Study 2016. *Lancet Neurol* **2019**, *18*, 376–393. doi:10.1016/s1474-4422(18)30468-x.

7. Louis, D. N.; Perry, A.; Wesseling, P.; Brat, D. J.; Cree, I. A.; Figarella-Branger, D.; Hawkins, C.; Ng, H. K.; Pfister, S. M.; Reifenberger, G.; Soffietti, R.; von Deimling, A.; Ellison, D. W. The 2021 WHO Classification of Tumors of the Central Nervous System: A Summary. *Neuro Oncol* **2021**, *23*, 1231-1251. doi:10.1093/neuonc/noab106.

8. Kleihues, P.; Ohgaki, H. Primary and Secondary Glioblastomas: From Concept to Clinical Diagnosis. *Neuro Oncol* **1999**, *1*, 44–51. doi: 10.1093/neuonc/1.1.44.

9. Ohgaki, H.; Kleihues, P. The Definition of Primary and Secondary Glioblastoma. *Clin. Cancer Res.* **2012**, *19*, 764–772. doi:10.1158/1078-0432.ccr-12-3002.

10. Mansouri, A.; Karamchandani, J.; Das, S. *Glioblastoma,* Codon Publications, 2017; Chapter 2. doi: 10.15586/codon.glioblastoma.2017.ch2.

11. Georgescu, M.-M. Multi-Platform Classification of IDH-Wild-Type Glioblastoma Based on ERK/MAPK Pathway: Diagnostic, Prognostic and Therapeutic Implications. *Cancers* **2021**, *13*, 4532. doi:10.3390/cancers13184532.

12. Cohen, A. L.; Holmen, S. L.; Colman, H. IDH1 and IDH2 Mutations in Gliomas. *Curr Neurol Neurosci Rep* **2013**, *13*, 345. doi:10.1007/s11910-013-0345-4.

13. Verhaak, R. G. W.; Hoadley, K. A.; Purdom, E.; Wang, V.; Qi, Y.; Wilkerson, M. D.; Miller, C. R.; Ding, L.; Golub, T.; Mesirov, J. P.; Alexe, G.; Lawrence, M.; O'Kelly, M.; Tamayo, P.; Weir, B. A.; Gabriel, S.; Winckler, W.; Gupta, S.; Jakkula, L.; Feiler, H. S. Integrated Genomic Analysis Identifies Clinically

Relevant Subtypes of Glioblastoma Characterized by Abnormalities in PDGFRA, IDH1, EGFR, and NF1. *Cancer Cell* **2010**, *17*, 98–110. doi:10.1016/j.ccr.2009.12.020.

14. Nakada, M.; Kita, D.; Watanabe, T.; Hayashi, Y.; Teng, L.; Pyko, I. V.; Hamada, J.-I. Aberrant Signaling Pathways in Glioma. *Cancers* **2011**, *3*, 3242–3278. doi:10.3390/cancers3033242.

15. Hanif, F.; Muzaffar, K.; Perveen, K.; Malhi, S. M.; Simjee, S. U. Glioblastoma Multiforme: A Review of Its Epidemiology and Pathogenesis through Clinical Presentation and Treatment. *Asian Pac. J. Cancer Prev* **2019**, *18*, 3–9. doi:10.22034/APJCP.2017.18.1.3.

16. Cloughesy, T. F.; Cavenee, W. K.; Mischel, P. S. Glioblastoma: From Molecular Pathology to Targeted Treatment. *Annu. Rev. Pathol.: Mech. Dis* **2014**, *9*, 1–25. doi:10.1146/annurev-pathol-011110-130324.

17. Tomaszewski, W.; Sanchez-Perez, L.; Gajewski, T. F.; Sampson, J. H. Brain Tumor Micro-Environment and Host State - Implications for Immunotherapy. *Clin. Cancer Res* **2019**, *25*, 4202-4210. doi:10.1158/1078-0432.ccr-18-1627.

18. D'Alessio, A.; Proietti, G.; Sica, G.; Scicchitano, B. M. Pathological and Molecular Features of Glioblastoma and Its Peritumoral Tissue. *Cancers* **2019**, *11*, 469. doi:10.3390/cancers11040469.

19. Davis, M. Glioblastoma: Overview of Disease and Treatment. *Clinical Journal of Oncology Nursing* **2016**, *20*, 2–8. doi:10.1188/16.cjon.s1.2-8.

20. Vagvala, S.; Guenette, J. P.; Jaimes, C.; Huang, R. Y. Imaging Diagnosis and Treatment Selection for Brain Tumors in the Era of Molecular Therapeutics. *Cancer Imaging* **2022**, *22*, 19. doi:10.1186/s40644-022-00455-5.

21. Abd-Elghany, A. A.; Naji, A. A.; Alonazi, B.; Aldosary, H.; Alsufayan, M. A.; Alnasser, M.; Mohammad, E. A.; Mahmoud, M. Z. Radiological Characteristics of Glioblastoma Multiforme Using CT and MRI Examination. *J. Radiat. Res. Appl. Sci.* **2019**, *12*, 289–293. doi:10.1080/16878507.2019.1655864.

22. Sulman, E. P.; Ismaila, N.; Armstrong, T. S.; Tsien, C.; Batchelor, T. T.; Cloughesy, T.; Galanis, E.; Gilbert, M.; Gondi, V.; Lovely, M.; Mehta, M.; Mumber, M. P.; Sloan, A.; Chang, S. M. Radiation Therapy for Glioblastoma: American Society of Clinical Oncology Clinical Practice Guideline Endorsement of the American Society for Radiation Oncology Guideline. *Clin Oncol* **2017**, *35*, 361–369. doi:10.1200/jco.2016.70.7562.

23. Gzell, C.; Back, M.; Wheeler, H.; Bailey, D.; Foote, M. Radiotherapy in Glioblastoma: The Past, the Present and the Future. *Clin Oncol* **2017**, *29*, 15–25. doi:10.1016/j.clon.2016.09.015.

24. Mann, J.; Ramakrishna, R.; Magge, R.; Wernicke, A. G. Advances in Radiotherapy for Glioblastoma. *Front Neurol* **2018**, *8,* 748. doi:/10.3389/fneur.2017.00748.

25. Roa, W.; Brasher, P. M. A.; Bauman, G.; Anthes, M.; Bruera, E.; Chan, A.; Fisher, B.; Fulton, D.; Gulavita, S.; Hao, C.; Husain, S.; Murtha, A.; Petruk, K.; Stewart, D.; Tai, P.; Urtasun, R.; Cairncross, J. G.; Forsyth, P. Abbreviated Course of Radiation Therapy in Older Patients with Glioblastoma Multiforme: A Prospective Randomized Clinical Trial. *Clin Oncol* **2004**, *22*, 1583–1588. doi:10.1200/jco.2004.06.082.

26. Stupp, R.; Mason, W. P.; van den Bent, M. J.; Weller, M.; Fisher, B.; Taphoorn, M. J. B.; Belanger, K.; Brandes, A. A.; Marosi, C.; Bogdahn, U.; Curschmann, J.; Janzer, R. C.; Ludwin, S. K.; Gorlia, T.; Allgeier, A.; Lacombe, D.; Cairncross, J. G.; Eisenhauer, E.; Mirimanoff, R. O.

Radiotherapy plus Concomitant and Adjuvant Temozolomide for Glioblastoma. *N. Engl. J. Med.* **2005**, *352*, 987–996. doi:10.1056/nejmoa043330.

27. Wenger, C.; Miranda, P. C.; Salvador, R.; Thielscher, A.; Bomzon, Z.; Giladi, M.; Mrugala, M. M.; Korshoej, A. R. A Review on Tumor-Treating Fields (TTFields): Clinical Implications Inferred from Computational Modeling. *IEEE Rev Biomed Eng* **2018**, *11*, 195–207. doi:10.1109/rbme.2017.2765282.

28. Stupp, R.; Taillibert, S.; Kanner, A.; Read, W.; Steinberg, D. M.; Lhermitte, B.; Toms, S.; Idbaih, A.; Ahluwalia, M. S.; Fink, K.; Di Meco, F.; Lieberman, F.; Zhu, J.-J.; Stragliotto, G.; Tran, D. D.; Brem, S.; Hottinger, A. F.; Kirson, E. D.; Lavy-Shahaf, G.; Weinberg, U. Effect of Tumor-Treating Fields plus Maintenance Temozolomide vs Maintenance Temozolomide Alone on Survival in Patients with Glioblastoma. *JAMA* **2017**, *318*, 2306. doi:10.1001/jama.2017.18718.

29. Bae, S. H.; Park, M.-J.; Lee, M. M.; Kim, T. M.; Lee, S.-H.; Cho, S. Y.; Kim, Y.-H.; Kim, Y. J.; Park, C.-K.; Kim, C.-Y. Toxicity Profile of Temozolomide in the Treatment of 300 Malignant Glioma Patients in Korea. *J. Korean Med. Sci* **2014**, *29*, 980. doi:10.3346/jkms.2014.29.7.980.

30. Wesolowski, J. R.; Rajdev, P.; Mukherji, S. K. Temozolomide (Temodar). *AJNR Am J Neuroradio* **2010**, *31*, 1383–1384. doi:10.3174/ajnr.a2170.

31. Quirbt, I., Verma, S., Petrella, T., Bak, K., Charette, M., Members of the Melanoma Disease Site Group of Cancer Care Ontario's Program in Evidence-Based Care. Temozolomide for the treatment of metastatic melanoma. Curr. Biol. **2007**, *14*, 27–33. doi:org/10.3747/co.2007.98.

32. Rubio-Camacho, M.; Encinar, J. A.; Martínez-Tomé, M. J.; Esquembre, R.; Mateo, C. R. The Interaction of Temozolomide with Blood Components

Suggests the Potential Use of Human Serum Albumin as a Biomimetic Carrier for the Drug. *Biomolecules* **2020**, *10*, 1015. doi:10.3390/biom10071015.

33. Newlands, E. S.; Stevens, M. F. G.; Wedge, S. R.; Wheelhouse, R. T.; Brock, C. Temozolomide: A Review of Its Discovery, Chemical Properties, Pre-Clinical Development and Clinical Trials. *Cancer Treat. Rev* **1997**, *23*, 35–61. doi:10.1016/s0305-7372(97)90019-0.

34. Friedman, H. S.; Kerby, T.; Calvert, H. Temozolomide and Treatment of Malignant Glioma. *Clin. Cancer Res* **2000**, *6*, 2585–2597. PMID: 10914698.

35. Denny, B. J.; Wheelhouse, R. T.; Stevens, M. F. G.; Tsang, L. L. H.; Slack, J. A. NMR and Molecular Modeling Investigation of the Mechanism of Activation of the Antitumor Drug Temozolomide and Its Interaction with DNA. *Biochemistry* **1994**, *33*, 9045–9051. doi:10.1021/bi00197a003.

36. Baker, S. D.; Wirth, M.; Statkevich, P.; Reidenberg, P.; Alton, K.; Sartorius, S. E.; Dugan, M.; Cutler, D.; Batra, V.; Grochow, L. B.; Donehower, R. C.; Rowinsky, E. K. Absorption, Metabolism, and Excretion of 14C-Temozolomide Following Oral Administration to Patients with Advanced Cancer. *Clin. Cancer Res.* **1999**, *5*, 309–317. PMID:10037179.

37. Singh, N.; Miner, A.; Hennis, L.; Mittal, S. Mechanisms of Temozolomide Resistance in Glioblastoma - a Comprehensive Review. *Cancer Drug Resist.* **2020**, *4*, 17-42. doi:10.20517/cdr.2020.79.

38. Yoshimoto, K.; Mizoguchi, M.; Hata, N.; Murata, H.; Hatae, R.; Amano, T.; Nakamizo, A.; Sasaki, T. Complex DNA Repair Pathways as Possible Therapeutic Targets to Overcome Temozolomide Resistance in Glioblastoma. *Front. Oncol* **2012**, *2*, 186. doi:10.3389/fonc.2012.00186.

39. Kaina, B.; Ochs, K.; Grösch, S.; Fritz, G.; Lips, J.; Tomicic, M.; Dunkern, T.; Christmann, M. BER, MGMT, and MMR in Defense against Alkylation-

Induced Genotoxicity and Apoptosis. *Prog. Nucleic Acid Res. Mol. Biol.* **2001**, *68*, 41–54. doi:10.1016/s0079-6603(01)68088-7.

40. Scaringi, C., De Sanctis, V., Minniti, G. and Enrici, R.M. Temozolomide-Related Hematologic Toxicity. *Oncol Res Treat* **2013**, *36*, 444–449. doi:10.1159/000353752.

41. Daneman, R.; Prat, A. The Blood–Brain Barrier. *Cold Spring Harb. Perspect. Biol.* **2015**, *7*, a020412. doi:10.1101/cshperspect.a020412.

42. Abbott, N.J. Dynamics of CNS Barriers: Evolution, Differentiation, and Modulation. *Cell. Mol. Neurobiol* **2005**, *25*, 5–23. doi:10.1007/s10571-004-1374-y.

43. Portnow, J.; Badie, B.; Chen, M.; Liu, A.; Blanchard, S.; Synold, T. W. THE NEUROPHARMACOKINETICS of TEMOZOLOMIDE in PATIENTS with RESECTABLE BRAIN TUMORS: POTENTIAL IMPLICATIONS for the CURRENT APPROACH to CHEMORADIATION. *Clin. Cancer Res.* **2009**, *15*, 7092–7098. doi:10.1158/1078-0432.CCR-09-1349.

44. Friedman, H. S.; McLendon, R. E.; Kerby, T.; Dugan, M.; Bigner, S. H.; Henry, A. J.; Ashley, D. M.; Krischer, J.; Lovell, S.; Rasheed, K.; Marchev, F.; Seman, A. J.; Cokgor, I.; Rich, J.; Stewart, E.; Colvin, O. M.; Provenzale, J. M.; Bigner, D. D.; Haglund, M. M.; Friedman, A. H. DNA Mismatch Repair and O6-Alkylguanine-DNA Alkyltransferase Analysis and Response to Temodal in Newly Diagnosed Malignant Glioma. *J Clin Oncol* **1998**, *16*, 3851–3857. doi:10.1200/JCO.1998.16.12.3851.

45. Weller, M.; Stupp, R.; Reifenberger, G.; Brandes, A. A.; van den Bent, M. J.; Wick, W.; Hegi, M. E. MGMT Promoter Methylation in Malignant Gliomas: Ready for Personalized Medicine? *Nat. Rev. Neurol.* **2009**, *6*, 39–51. doi:10.1038/nrneurol.2009.197.

46. Esteller, M.; Herman, J. G. Generating Mutations but Providing Chemosensitivity: The Role of O6-Methylguanine DNA Methyltransferase in Human Cancer. *Oncogene* **2004**, *23*, 1–8. doi:10.1038/sj.onc.1207316.

47. Jefferies, W. A.; Brandon, M. R.; Hunt, S. V.; Williams, A. F.; Gatter, K. C.; Mason, D. Y. Transferrin Receptor on Endothelium of Brain Capillaries. *Nature* **1984**, *312*, 162–163. doi:10.1038/312162a0.

48. Anthony, D. P.; Hegde, M.; Shetty, S. S.; Rafic, T.; Mutalik, S.; Rao, B. S. S. Targeting Receptor-Ligand Chemistry for Drug Delivery across Blood-Brain Barrier in Brain Diseases. *Life Sci* **2021**, *274*, 119326. doi:10.1016/j.lfs.2021.119326.

49. Andrews, S. C.; Arosio, P.; Bottke, W.; Briat, J. F.; von Darl, M.; Harrison, P. M.; Laulhère, J. P.; Levi, S.; Lobreaux, S.; Yewdall, S. J. Structure, Function, and Evolution of Ferritins. *J Inorg Biochem* **1992**, *47*, 161–174. doi:10.1016/0162-0134(92)84062-r.

50. Macara, I.G., Hoy, T.G. and Harrison, P.M. The formation of ferritin from apoferritin. Kinetics and mechanism of iron uptake. *Biochem* **1972**, *126*, 151–162. doi:10.1042/bj1260151.

51. Boyd, D., Vecoli, C., Belcher, D.M., Jain, S.K. and Drysdale, J.W. Structural and functional relationships of human ferritin H and L chains deduced from cDNA clones. *J. Biol Chem* **1985**, *260*, 11755–11761. doi:10.1016/S0021-9258(17)39094-4.

52. Yin, S.; Davey, K.; Dai, S.; Liu, Y.; Bi, J. A Critical Review of Ferritin as a Drug Nanocarrier: Structure, Properties, Comparative Advantages and Challenges. *Particuology* **2021**, *64*, 65-84. doi:10.1016/j.partic.2021.04.020.

53. Liu, X., Jin, W. and Theil, E.C. Opening protein pores with chaotropes enhances Fe reduction and chelation of Fe from the ferritin biomineral. *Proc. Natl. Acad. Sci. U.S.A.* **2003**, *100*, 3653–3658. doi:10.1073/pnas.0636928100.

54. Dostalova, S., Vasickova, K., Hynek, D., Krizkova, S., Richtera, L., Vaculovicova, M., Eckschlager, T., Stiborova, M., Heger, Z. and Adam, V. Apoferritin as an ubiquitous nanocarrier with excellent shelf life. *Int J Nanomedicine* **2017**, *12*, 2265–2278. doi:10.2147/IJN.S130267.

55. Kim, M., Rho, Y., Jin, K.S., Ahn, B., Jung, S., Kim, H. and Ree, M. pH-Dependent Structures of Ferritin and Apoferritin in Solution: Disassembly and Reassembly. *Biomacromolecules* **2011**, *12*, 1629–1640. doi:10.1021/bm200026v.

56. Heger, Z., Skalickova, S., Zitka, O., Adam, V. and Kizek, R. Apoferritin applications in nanomedicine. *Nanomed. J* **2014**, *9*, 2233–2245. doi:10.2217/nnm.14.119.

57. Song, N., Zhang, J., Zhai, J., Hong, J., Yuan, C. and Liang, M. Ferritin: A Multifunctional Nanoplatform for Biological Detection, Imaging Diagnosis, and Drug Delivery. *Acc. Chem. Res.* **2021**, *54*, pp.3313–3325. doi:10.1021/acs.accounts.1c00267.

58. Fan, K., Jia, X., Zhou, M., Wang, K., Conde, J., He, J., Tian, J. and Yan, X. Ferritin Nanocarrier Traverses the Blood Brain Barrier and Kills Glioma. *ACS Nano* **2018**, *12*, 4105–4115. doi:10.1021/acsnano.7b06969.

59. Li, L., Fang, C.J., Ryan, J.C., Niemi, E.C., Lebrón, J.A., Björkman, P.J., Arase, H., Torti, F.M., Torti, S.V., Nakamura, M.C. and Seaman, W.E. Binding and uptake of H-ferritin are mediated by human transferrin receptor-1. *Proc. Natl. Acad. Sci. U.S.A.* **2010**, *107*, 3505–3510. doi:10.1073/pnas.0913192107.

60. He, D. and Marles-Wright, J. Ferritin family proteins and their use in bionanotechnology. *N Biotechnol* **2015**, *32*, 651–657. doi:10.1016/j.nbt.2014.12.006

61. Zhang, L. Multifunctional Apoferritin and Dps Protein Nanoparticles for In Vivo Imaging and Breast Cancer Treatment. *University of Nottingham* **2015**.

62. Lemmon, M.A. and Schlessinger, J. Cell Signaling by Receptor Tyrosine Kinases. *Cell* **2010**, *141*, 1117–1134. doi:10.1016/j.cell.2010.06.011.

63. Hubbard, S.R. Structural analysis of receptor tyrosine kinases. *Prog. Biophys. Mol. Biol.* **1999**, *71*, 343–358. doi:10.1016/s0079-6107(98)00047-9.

64. Paul, M.K. and Mukhopadhyay, A.K. Tyrosine kinase – Role and significance in Cancer. *Int. J. Med. Sci.* **2004**, *1*, 101–115. doi:10.7150/ijms.1.101.

65. Ullrich, A. and Schlessinger, J. Signal transduction by receptors with tyrosine kinase activity. *Cell* **1990**, *61*, 203–212. doi:10.1016/0092-8674(90)90801-k.

66. Li, E. and Hristova, K. Role of Receptor Tyrosine Kinase Transmembrane Domains in Cell Signaling and Human Pathologies. *Biochemistry* **2006**, *45*, 6241–6251. doi:10.1021/bi060609y.

67. Hedger, G., Sansom, M.S.P. and Koldsø, H. The juxtamembrane regions of human receptor tyrosine kinases exhibit conserved interaction sites with anionic lipids. *Sci. Rep.* **2015**, *5*, 9198. doi:10.1038/srep09198.

68. Ceresa, B.P. and Peterson, J.L. Cell and molecular biology of epidermal growth factor receptor. *Int Rev Cell Mol Biol* **2014**, *313*, 145–178. doi:10.1016/B978-0-12-800177-6.00005-0.

69. Arteaga, C.L. and Engelman, J.A. ERBB receptors: From oncogene discovery to basic science to mechanism-based cancer therapeutics. *Cancer cell* **2014**, *25*, 282–303. doi:10.1016/j.ccr.2014.02.025.

70. Appert-Collin, A., Hubert, P., Crémel, G. and Bennasroune, A. Role of ErbB Receptors in Cancer Cell Migration and Invasion. *Front. Pharmacol.* **2015**, *6*, 283. doi:10.3389/fphar.2015.00283.

71. Du, Z. and Lovly, C.M. (2018). Mechanisms of receptor tyrosine kinase activation in cancer. *Mol. Cancer* **2018**, *17*, 101-115. doi:10.1186/s12943-018-0782-4.

72. Ferguson, K.M., Berger, M.B., Mendrola, J.M., Cho, H.-S., Leahy, D.J. and Lemmon, M.A. EGF Activates Its Receptor by Removing Interactions that Autoinhibit Ectodomain Dimerization. *Mol. Cell* **2003**, *11*, 507–517. doi:10.1016/s1097-2765(03)00047-9.

73. Oprita, A., Baloi, S.-C., Staicu, G.-A., Alexandru, O., Tache, D.E., Danoiu, S., Micu, E.S. and Sevastre, A.-S. Updated Insights on EGFR Signaling Pathways in Glioma. *Int. J. Mol. Sci.* **2021**, *22*, 587. doi:10.3390/ijms22020587.

74. Leahy, D.J. The Ins and Outs of EGFR Asymmetry. *Cell* **2010**, *142*, 513–515. doi:10.1016/j.cell.2010.08.003.

75. Roskoski, R. ErbB/HER protein-tyrosine kinases: Structures and small molecule inhibitors. *Pharmacol. Res.* **2014**, *87*, 42–59. doi:10.1016/j.phrs.2014.06.001.

76. Mellman, I. and Yarden, Y. Endocytosis and Cancer. *Cold Spring Harb. Perspect. Biol.* **2013**, *5*, a016949. doi:10.1101/cshperspect.a016949.

77. Uhlén, M., Guss, B., Nilsson, B., Gatenbeck, S., Philipson, L. and Lindberg, M. Complete sequence of the staphylococcal gene encoding protein A. A gene evolved through multiple duplications. *J. Biol. Chem.* **1984**, *259*, 1695–1702. PMID: 6319407

78. Ståhl, S., Gräslund, T., Eriksson Karlström, A., Frejd, F.Y., Nygren, P.-Å. and Löfblom, J. Affibody Molecules in Biotechnological and Medical Applications. *Trends Biotechnol.* **2017**, *35*, 691–712. doi:10.1016/j.tibtech.2017.04.007.

79. Nygren, P.-Å. Alternative binding proteins: Affibody binding proteins developed from a small three-helix bundle scaffold. *FEBS J.* **2008**, *275*, 2668–2676. doi:10.1111/j.1742-4658.2008.06438.x.

80. Chung, W.K., Russell, B., Yang, Y., Handlogten, M., Hudak, S., Cao, M., Wang, J., Robbins, D., Ahuja, S. and Zhu, M. Effects of antibody disulfide bond reduction on purification process performance and final drug substance stability. *Biotechnol. Bioeng.* **2017**, *114*, 1264–1274. doi:10.1002/bit.26265.

81. Löfblom, J., Feldwisch, J., Tolmachev, V., Carlsson, J., Ståhl, S. and Frejd, F.Y. Affibody molecules: Engineered proteins for therapeutic, diagnostic and biotechnological applications. *FEBS L.* **2010**, *584*, 2670–2680. doi:10.1016/j.febslet.2010.04.014.

82. Tolmachev, V., Orlova, A., Nilsson, F.Y., Feldwisch, J., Wennborg, A. and Abrahmsén, L. (2007). Affibody molecules: potential for in vivo imaging of molecular targets for cancer therapy. *Expert Opin. Biol. Ther.* **2007**, *7*, 555–568. doi:10.1517/14712598.7.4.555.

83. Kronqvist, N., Malm, M., Göstring, L., Gunneriusson, E., Nilsson, M., Höidén Guthenberg, I., Gedda, L., Frejd, F.Y., Ståhl, S. and Löfblom, J. Combining phage and staphylococcal surface display for generation of ErbB3-specific Affibody molecules. *Protein Eng. Des. Sel.* **2011**, *24*, 385–396. doi:10.1093/protein/gzq118.

84. Dostalova, S., Cerna, T., Hynek, D., Koudelkova, Z., Vaculovic, T., Kopel, P., Hrabeta, J., Heger, Z., Vaculovicova, M., Eckschlager, T., Stiborova, M. and

Adam, V. Site-Directed Conjugation of Antibodies to Apoferritin Nanocarrier for Targeted Drug Delivery to Prostate Cancer Cells. *ACS Appl. Mater. Interfaces* **2016**, *8*, 14430–14441. doi:10.1021/acsami.6b04286.

85. Bouzinab, K., Summers, H.S., Stevens, M.F.G., Moody, C.J., Thomas, N.R., Gershkovich, P., Weston, N., Ashford, M.B., Bradshaw, T.D. and Turyanska, L. Delivery of Temozolomide and N3-Propargyl Analog to Brain Tumors Using an Apoferritin Nanocage. *ACS Appl. Mater. Interfaces* **2020**, *12*, 12609–12617. doi:10.1021/acsami.0c01514.

86. Tolmachev, V., Friedman, M., Sandström, M., Eriksson, T.L.J., Rosik, D., Hodik, M., Ståhl, S., Frejd, F.Y. and Orlova, A. Affibody molecules for epidermal growth factor receptor targeting in vivo: aspects of dimerization and labeling chemistry. *J. Nucl. Med.* **2009**, *50*, 274–283. doi:10.2967/jnumed.108.055525.

87. Tolmachev, V., Rosik, D., Wållberg, H., Sjöberg, A., Sandström, M., Hansson, M., Wennborg, A. and Orlova, A. Imaging of EGFR expression in murine xenografts using site-specifically labelled anti-EGFR 111In-DOTA-ZEGFR:2377 Affibody molecule: aspect of the injected tracer amount. *Eur. J. Nucl. Med. Mol. Imaging.* **2009**, *37*, 613–622. doi:10.1007/s00259-009-1283-x.

88. Friedman, M., Orlova, A., Johansson, E., Eriksson, T.L.J., Höidén-Guthenberg, I., Tolmachev, V., Nilsson, F.Y. and Ståhl, S. Directed Evolution to Low Nanomolar Affinity of a Tumor-Targeting Epidermal Growth Factor Receptor-Binding Affibody Molecule. *J. Mol. Biol.* **2008**, *376*, 1388–1402. doi:10.1016/j.jmb.2007.12.060.

89. Rosano, G. L., Ceccarelli, E. A. Recombinant Protein Expression in Escherichia Coli: Advances and Challenges. *Front. Microbiol.* **2014**, *5*, 172. doi:10.3389/fmicb.2014.00172.

90. Spriestersbach, A.; Kubicek, J.; Schäfer, F.; Block, H.; Maertens, B. Purification of His-Tagged Proteins. *Meth. Enzymol.* **2015**, *559*, 1–15. doi: 10.1016/bs.mie.2014.11.003.

91. Shi, H., Guo, Y., Liu, Y., Shi, B., Guo, X., Jin, L. and Yan, S. The in vitro effect of lipopolysaccharide on proliferation, inflammatory factors and antioxidant enzyme activity in bovine mammary epithelial cells. *Anim Nutr* **2016**, *2*, 99–104. doi:10.1016/j.aninu.2016.03.005.

92. Holden, I., PhD thesis not submitted at the time of submission of this thesis, *University of Nottingham* **2022**.

93. HiTrap™ chelating HP column manual, available at https://www.scientificlabs.co.uk/handlers/libraryFiles.ashx?filename=Manuals_1_17040801_A.PDF

94. Protein Calculator v3.4, available at https://protcalc.sourceforge.net/.

95. Wu, Y., Wu, M., He, G., Zhang, X., Li, W., Gao, Y., Li, Z., Wang, Z. and Zhang, C. Glyceraldehyde-3-phosphate dehydrogenase: A universal internal control for Western blots in prokaryotic and eukaryotic cells. *Anal. Biochem.* **2012**, *423*, 15–22. doi:10.1016/j.ab.2012.01.012.

96. Kim, S.-S.; Rait, A.; Kim, E.; DeMarco, J.; Pirollo, K. F.; Chang, E. H. Encapsulation of Temozolomide in a Tumor-Targeting Nanocomplex Enhances Anti-Cancer Efficacy and Reduces Toxicity in a Mouse Model of Glioblastoma. *Cancer Lett.* **2015**, *369*, 250–258. doi:10.1016/j.canlet.2015.08.022.

97. Tomas, A., Futter, C.E. and Eden, E.R. EGF receptor trafficking: consequences for signaling and cancer. *Trends Cell Biol.* **2014**, *24*, 26–34. doi:10.1016/j.tcb.2013.11.002.

98. Ni, X.-R., Zhao, Y.-Y., Cai, H.-P., Yu, Z.-H., Wang, J.; Chen, F.-R.; Yu, Y.-J.; Feng, G.-K.; Chen, Z.-P. Transferrin Receptor 1 Targeted Optical Imaging for Identifying Glioma Margin in Mouse Models. *J. Neuro-Oncol.* **2020**, *148*, 245–258. doi:10.1007/s11060-020-03527-3.

99. Cutrin, J.C., Alberti, D., Bernacchioni, C., Ciambellotti, S., Turano, P., Luchinat, C., Crich, S.G. and Aime, S. Cancer cell death induced by ferritins and the peculiar role of their labile iron pool. *Oncotarget* **2018**, *9*, 27974–27984. doi:10.18632/oncotarget.25416.

100. Puck, T., Marcus, P. Action of x-rays on mammalian cells. *J Exp Med.* **1957**, *103*, 653-666. doi:10.1084/jem.106.4.485.

101. Zi, Z. and Klipp, E. Cellular signaling is potentially regulated by cell density in receptor trafficking networks. FEBS Letters, **2007**, *581*, 4589-4595. doi:10.1016/j.febslet.2007.08.047

102. N.A.P., Rodermond, H.M., Stap, J., Haveman, J. and van Bree, C. Clonogenic assay of cells in vitro. *Nat. Protoc.* **2006**, *1*, 2315–2319. doi:10.1038/nprot.2006.339.

103. de las Alas, M.M., Aebi, S., Fink, D., Howell, S.B. and Los, G. Loss of DNA mismatch repair: effects on the rate of mutation to drug resistance. *J. Natl. Cancer Inst.* **1997**, *89*, 1537–1541. doi:10.1093/jnci/89.20.1537.

104. Ivashkevich, A. N.; Martin, O. A.; Smith, A. J.; Redon, C. E.; Bonner, W. M.; Martin, R. F.; Lobachevsky, P. N. ΓH2AX Foci as a Measure of DNA Damage: A Computational Approach to Automatic Analysis. *Mutat. Res.* **2011**, *711*, 49–60. doi:10.1016/j.mrfmmm.2010.12.015.

105. Yan, Y.; Xu, Z.; Dai, S.; Qian, L.; Sun, L.; Gong, Z. Targeting Autophagy to Sensitive Glioma to Temozolomide Treatment. *J. Exp. Clin. Cancer Res.* **2016**, *35*, 23. doi:10.1186/s13046-016-0303-5.

106. Kanzawa, T.; Germano, I. M.; Komata, T.; Ito, H.; Kondo, Y.; Kondo, S. Role of Autophagy in Temozolomide-Induced Cytotoxicity for Malignant Glioma Cells. *Cell Death & Differentiation* **2004**, *11*, 448–457, doi:10.1038/sj.cdd.4401359.

107. Kepp, O.; Galluzzi, L.; Lipinski, M.; Yuan, J.; Kroemer, G. Cell Death Assays for Drug Discovery. *Nat. Rev. Drug Discov* **2011**, *10*, 221–237. doi:org/10.1038/nrd3373.

108. Zhang, J., Hummersone, M., Matthews, C.S., Stevens, M.F.G. and Bradshaw, T.D. *N*3-Substituted Temozolomide Analogs Overcome Methylguanine-DNA Methyltransferase and Mismatch Repair Precipitating Apoptotic and Autophagic Cancer Cell Death. *Oncology* **2015**, *88*, 28–48. doi:10.1159/000366131.

7. Appendix

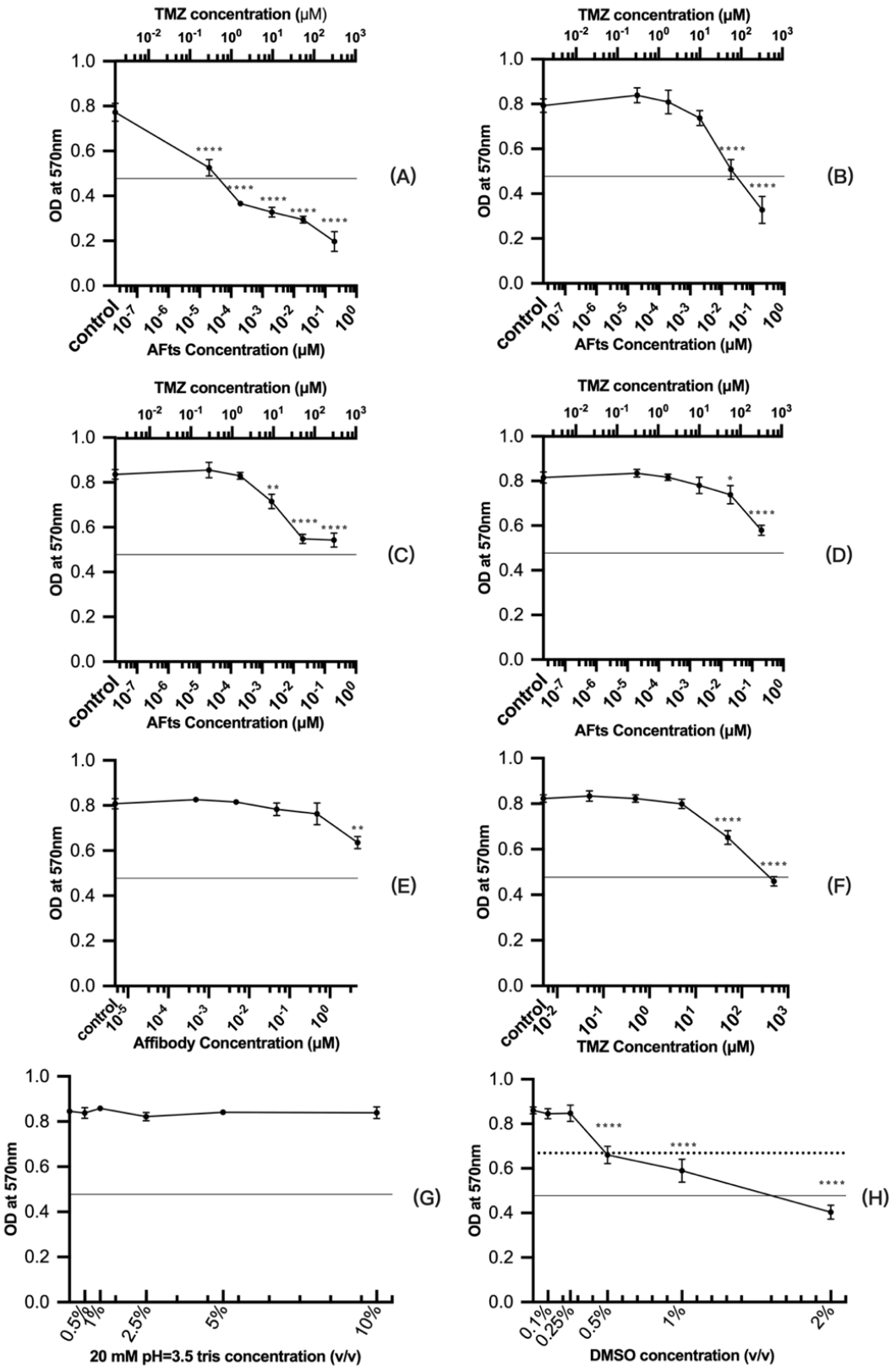
All growth-inhibition profiles mentioned in **4.4.1** are listed below. In each graph:

- **For 72 h assays, the label of each graph is summarised:** (A) EGFRa@AFt-TMZ, (B) AFt-TMZ, (C) EGFRa@AFt, (D) AFt, (E) EGFR-affibody, (F) TMZ, (G) tris buffer (20 mM, pH 3.5), (H) DMSO.

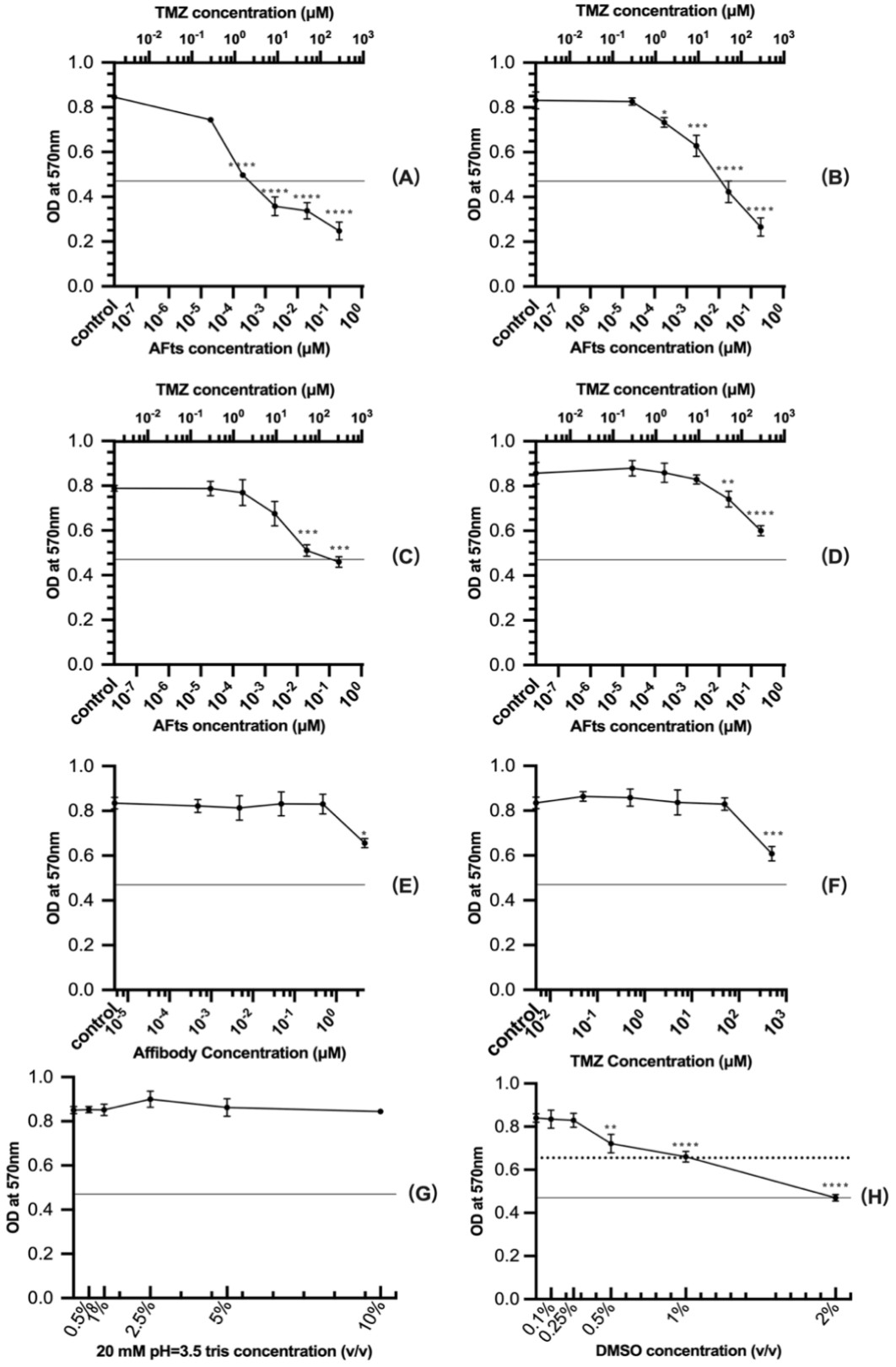
- **For 144 h assays, the labels represent:** (A) EGFRa@AFt-TMZ, (B) EGFRa@AFt, (C) TMZ. (D) DMSO, (E) tris buffer (20 mM, pH 3.5).

- Data were reported as mean ± SD (n=5, 3 trials were repeated), values of *P < 0.05, **P < 0.01, ***P < 0.001, and ****P < 0.0001 were considered as statistically significant compared to the control group.

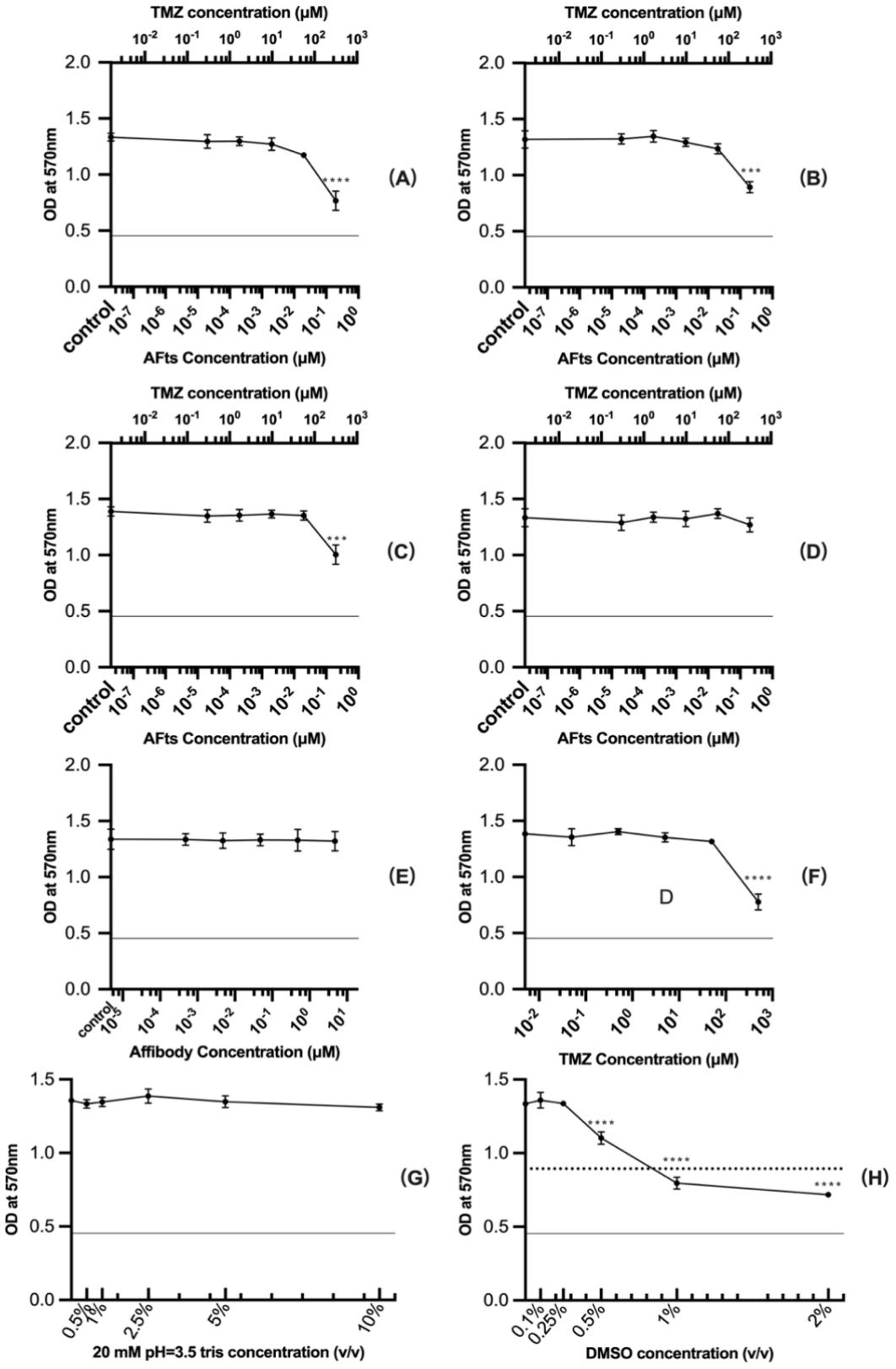
72 h assays:



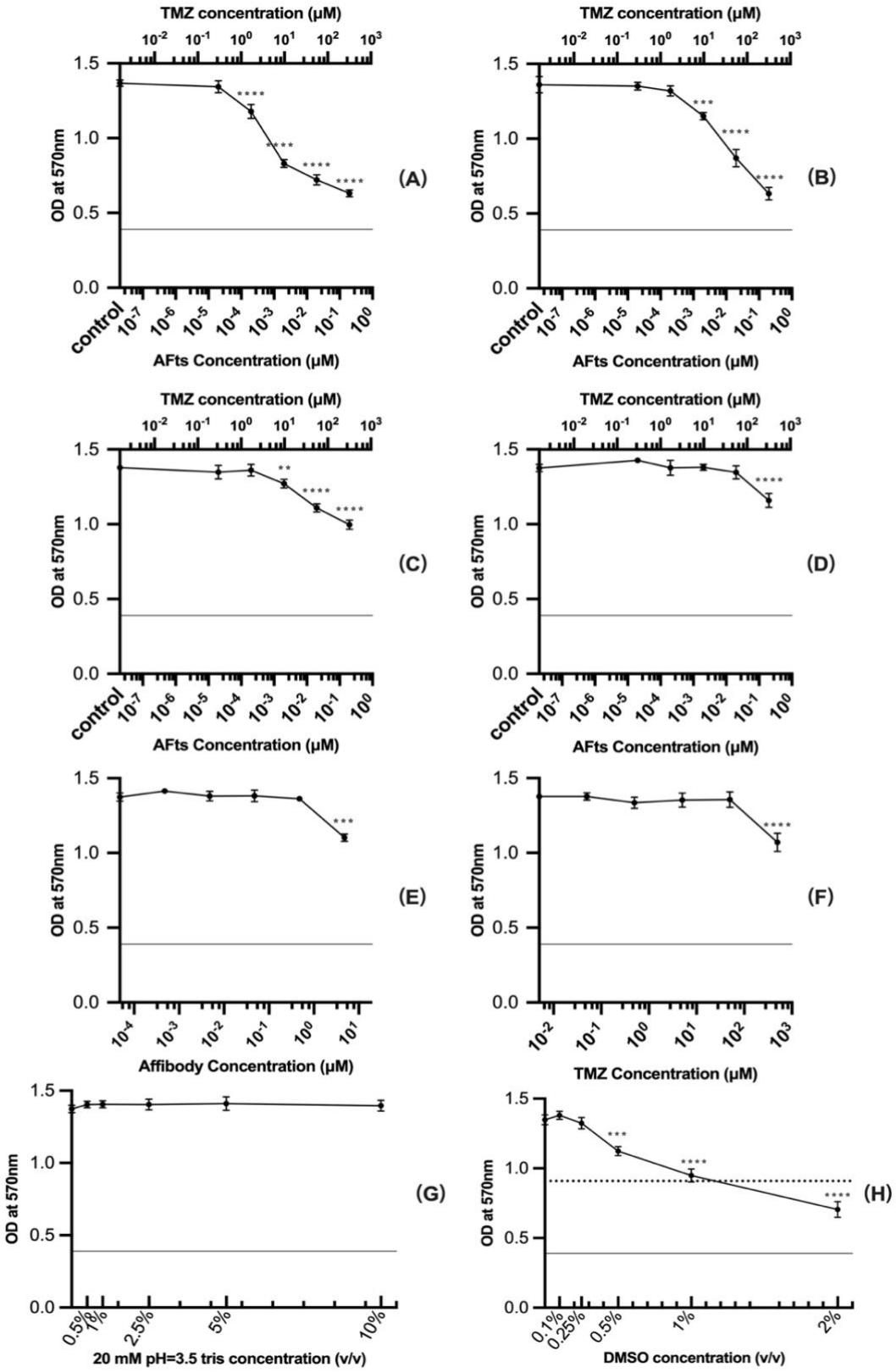
(U373V)


TMZ concentration (μM)
OD at 570nm
AFts concentration (μM)
(A)
(B)
AFts oncentration (μM)
(C)
(D)
Affibody Concentration (μM)
(E)
(F)
TMZ Concentration (μM)
20 mM pH=3.5 tris concentration (v/v)
(G)
DMSO concentration (v/v)
(H)

(U373M)

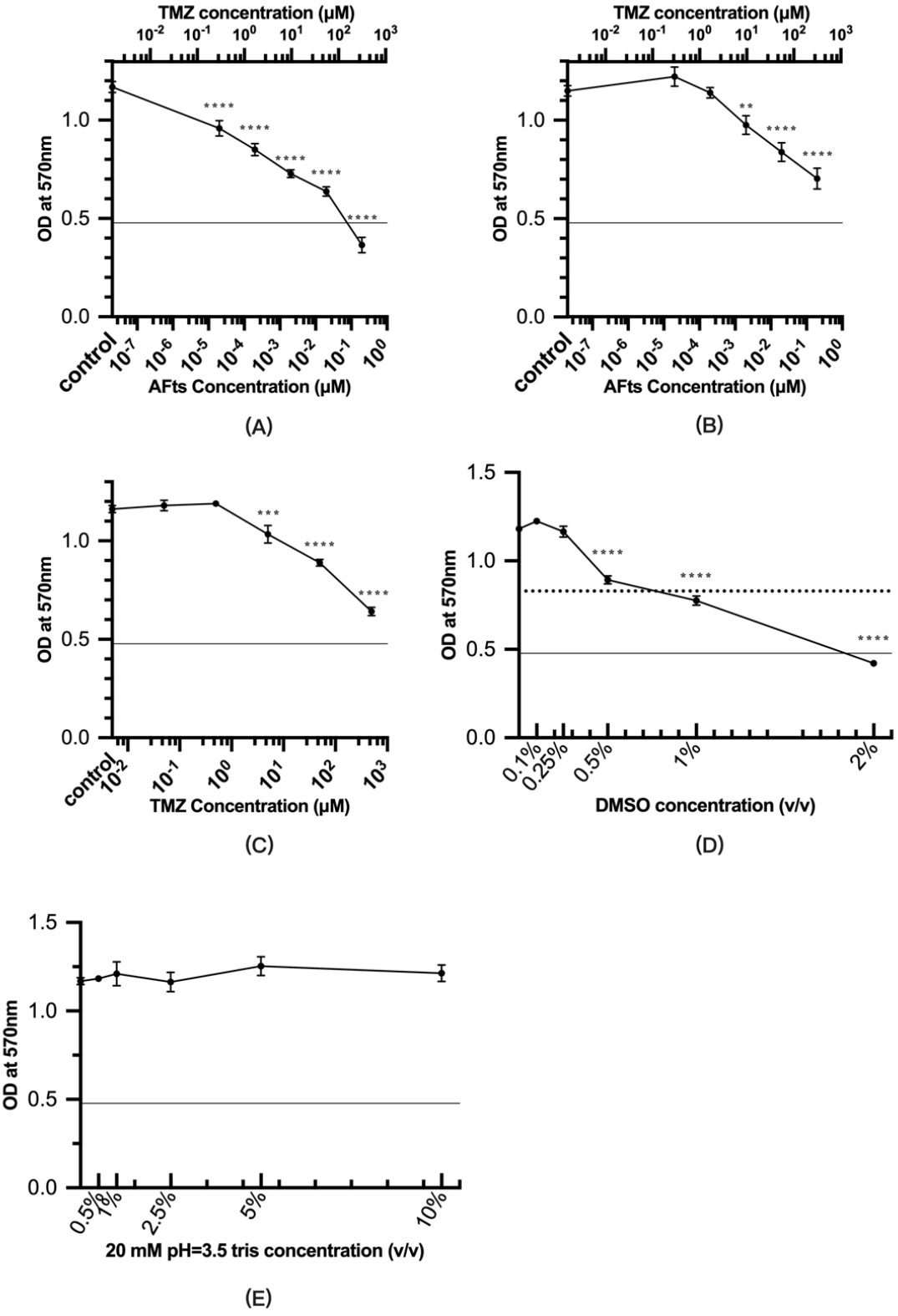

TMZ concentration (μM)
OD at 570nm
AFts Concentration (μM)
control
(A)
(B)
(C)
(D)
(E)
(F)
(G)
(H)
Affibody Concentration (μM)
TMZ Concentration (μM)
20 mM pH=3.5 tris concentration (v/v)
DMSO concentration (v/v)

(MRC-5)

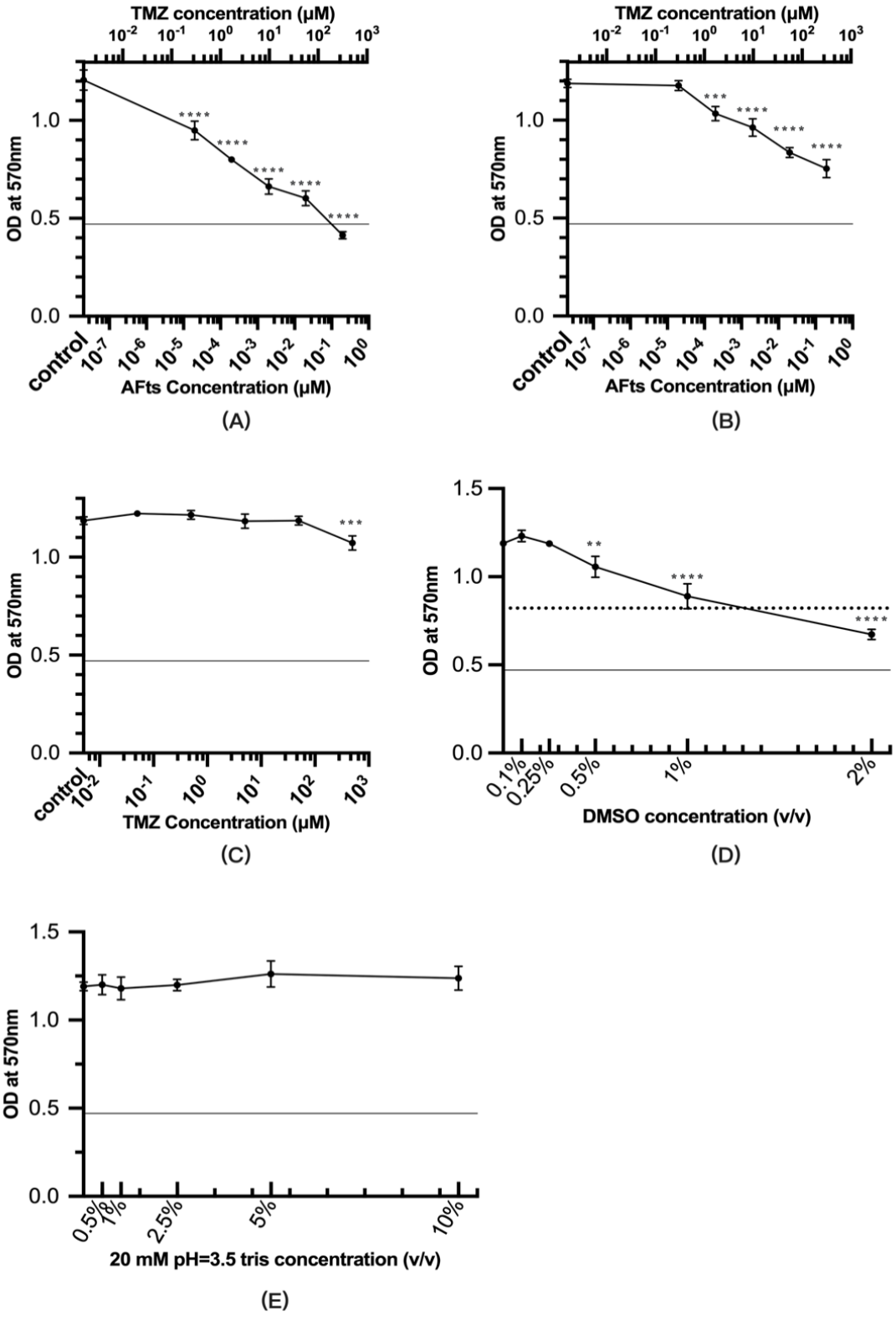

TMZ concentration (μM)
OD at 570nm
(A)
(B)
(C)
(D)
AFts Concentration (μM)
(E)
(F)
Affibody Concentration (μM)
TMZ Concentration (μM)
(G)
20 mM pH=3.5 tris concentration (v/v)
(H)
DMSO concentration (v/v)

(HCT-116)

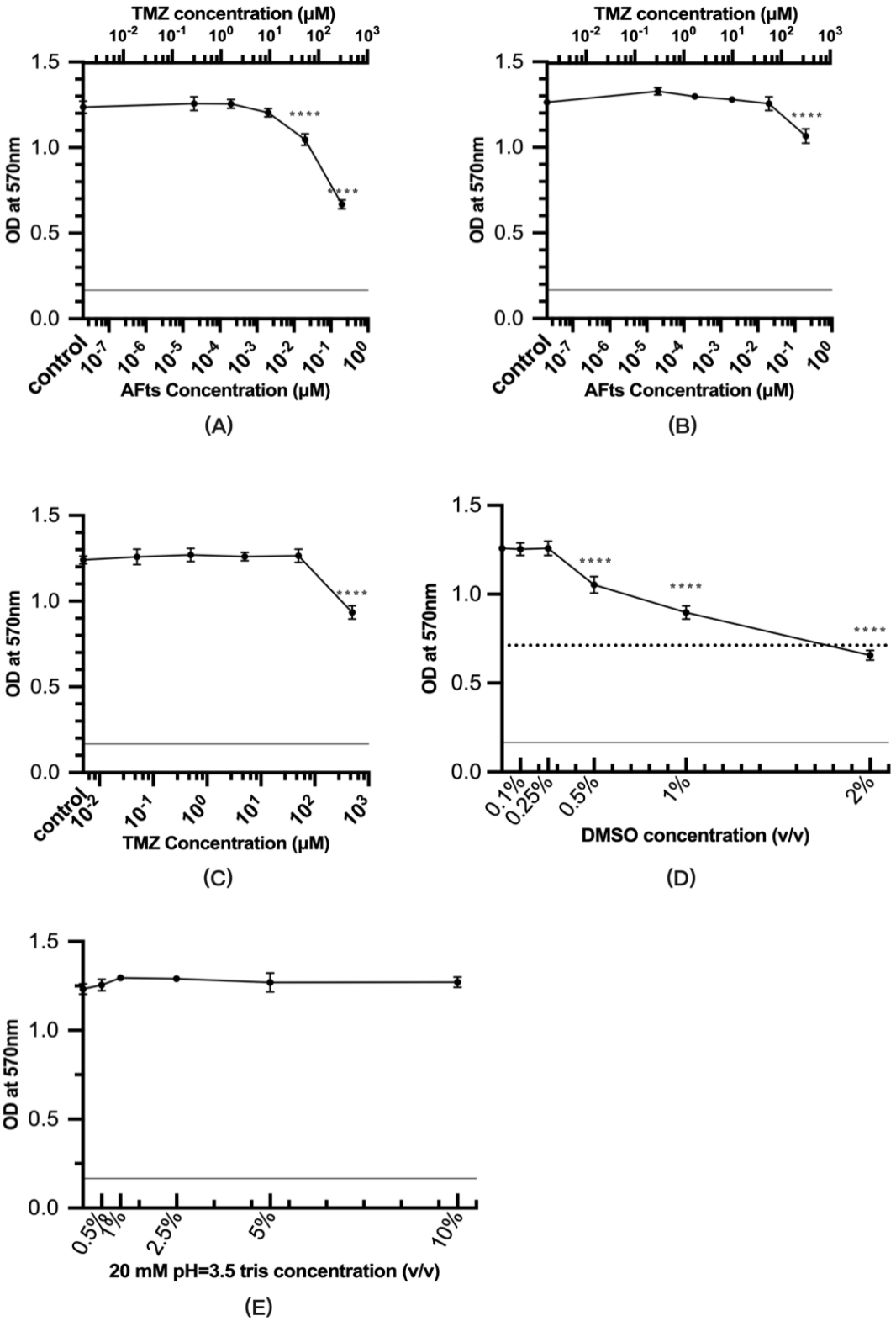
144 h assays:



(U373V)


TMZ concentration (μM)
OD at 570nm
AFts Concentration (μM)
(A)
(B)
TMZ Concentration (μM)
(C)
DMSO concentration (v/v)
(D)
20 mM pH=3.5 tris concentration (v/v)
(E)

(U373M)


TMZ concentration (μM)
OD at 570nm
AFts Concentration (μM)
(A)
(B)
TMZ Concentration (μM)
(C)
DMSO concentration (v/v)
(D)
20 mM pH=3.5 tris concentration (v/v)
(E)

(MRC-5)